1996

Characterization of neutron spectra at high energy electron accelerators

Le-Xuan Thai
San Jose State University

INFORMATION TO USERS

This manuscript has been reproduced from the microfilm master. UMI films the text directly from the original or copy submitted. Thus, some thesis and dissertation copies are in typewriter face, while others may be from any type of computer printer.

The quality of this reproduction is dependent upon the quality of the copy submitted. Broken or indistinct print, colored or poor quality illustrations and photographs, print bleedthrough, substandard margins, and improper alignment can adversely affect reproduction.

In the unlikely event that the author did not send UMI a complete manuscript and there are missing pages, these will be noted. Also, if unauthorized copyright material had to be removed, a note will indicate the deletion.

Oversize materials (e.g., maps, drawings, charts) are reproduced by sectioning the original, beginning at the upper left-hand corner and continuing from left to right in equal sections with small overlaps. Each original is also photographed in one exposure and is included in reduced form at the back of the book.

Photographs included in the original manuscript have been reproduced xerographically in this copy. Higher quality 6" x 9" black and white photographic prints are available for any photographs or illustrations appearing in this copy for an additional charge. Contact UMI directly to order.

UMI

A Bell & Howell Information Company
300 North Zeeb Road, Ann Arbor MI 48106-1346 USA
313/761-4700 800/521-0600

CHARACTERIZATION OF NEUTRON SPECTRA AT HIGH ENERGY ELECTRON ACCELERATORS

A Thesis

Presented to
The Nuclear Science Faculty
San Jose State University

In Partial Fulfillment
of the Requirements for the Degree
Master of Science

By
Le-Xuan Thai
May, 1996

APPROVED FOR THE NUCLEAR SCIENCE FACILITY

Dr. Allen Tucker

Dr. Vaclav Vylet

Dr. Adrian Rodriguez

APPROVED FOR THE UNIVERSITY

ABSTRACT

CHARACTERIZATION OF NEUTRON SPECTRA AT HIGH ENERGY ELECTRON ACCELERATORS

by Le-Xuan Thai

The purpose of this paper is to report the measurements of neutron spectra outside shielding of high energy electron accelerators, with a special emphasis on the high energy (above 20 MeV) portion. The detector system used in this work consists of the following:

- A standard set of Bonner spheres;
- A 12 inch sphere with 1 cm inner layer of lead; and
- A 5 inch by 5 inch plastic scintillator.

In addition, a pair of rem meters, one standard Anderson-Braun (AB) and one AB with an inner layer of lead (ABPB), were used. Neutron measurements were carried out at Stanford Linear Accelerator Center (SLAC) around facilities with various electron beam energies: 120 MeV, 2.3 GeV, and 46.6 GeV. Most of measured spectra show a high energy portion, i.e. neutrons with energies above 20 MeV.

ACKNOWLEDGMENTS

I am grateful to Drs. Vylet, Liu and Rokni from the Radiation Physics department at the Stanford Linear Accelerator Center for giving me the opportunity to participate in this series of measurements. I am indebted to Dr. James Liu for introducing me to and helping me with the ^{11}C activation method. My special thanks go to Dr. Vaclav Vylet, who introduced me to methods of neutron detection and spectrometry, assisted in all calibrations and measurements, and provided overall guidance of this thesis. I am grateful to Mr. Norman McElroy for proofreading this thesis and making helpful suggestions.

I also appreciate the help of Mr. Ron Seefred for help with instrumentation during calibration measurements, and the cooperation of the SSRL operators during the measurements at SPEAR and Linac.

TABLE OF CONTENTS

LIST OF FIGURES

LIST OF TABLES

CHAPTER 1: INTRODUCTION

1.1 INTRODUCTION

In comparison with photon dosimetry, neutron dosimetry presents more challenges for several reasons. Typical neutron fields span many decades of energy, usually 10^{-7} to 10^{7} MeV. Most neutron instruments cover only a small portion of this energy range. Fluence-to-dose equivalent conversion factors vary widely with neutron energy. Thus, an instrument sensitive only to fluence is inadequate for determining the dose equivalent. Therefore, it is useful to measure the neutron spectrum. Around high energy accelerators, neutron dosimetry is even more difficult because there are few suitable detectors for high energy neutrons. The sensitivity of most instruments used to measure neutrons falls for neutrons with energies beginning in the range of 15 MeV to 20 MeV and higher.

The purpose of this work is to determine neutron spectra outside shielding of high energy electron accelerators at the Stanford Linear Accelerator Center (SLAC), with a special emphasis on the high energy (>20 MeV) portion of the spectra. This was accomplished using a combination of the standard set of Bonner spheres plus a 12" sphere with lead, and a ^{12}C plastic scintillator. In addition to the above detector system, a pair of rem meters was also used: one standard Anderson-Braun, and one with an inner layer of lead that has an extended energy response. The derived dose equivalent rates of the detector system will be compared with those measured using the rem meters.

It is clear that all the work connected with a large measurement program such as this, i.e. transport, setup and use of bulky instrumentation, planning, scheduling and interacting with machine operators, could not have been handled by a single person. This work was done in collaboration with members of the Radiation Physics

Department at SLAC. The author's contribution consists of calibrating the Bonner sphere system and the rem meters, participating in all spectra measurements and performing the data analysis.

1.2 STANFORD LINEAR ACCELERATOR CENTER (SLAC)

SLAC has a two-mile-long linear accelerator that accelerates electron and positron beams up to energies of 50 GeV. These beams can be sent to different fixed target experiments in End Station A, and to the Final Focus Test Beam Facility (FFTB). Besides the fixed target experiments, a different mode of operation allows the operator to send electrons and positrons into two separate beam lines. Electron and positron beams are lead from opposite directions into the SLC (Stanford Linear Collider) and made to collide in the SLD (Stanford Large Detector).

A separate accelerator facility located at SLAC is the Stanford Synchrotron Radiation Laboratory (SSRL). It provides users with synchrotron radiation in several experimental beamlines. It has its own electron linear accelerator, a booster synchrotron, and an electron storage ring.

Although all the above facilities use electron beams, due to the very high energy of the electrons, neutrons are produced when these beams strike beam line components and beam dumps. Mechanisms of neutron production are described below.

1.3 NEUTRON PRODUCTION MECHANISMS

In an electron accelerator facility, when a high energy electron hits a target, a large fraction of the energy is spent in the production of high energy photons or bremsstrahlung, and only a small fraction of the energy is dissipated as a result of collision processes. Neutrons are produced when high energy photons interact with any material. Depending on the energy of the interacting photons, neutrons can be divided

into three groups: giant resonance (below 30 MeV), pseudo-deuteron (about 30-300 MeV), and photopion group (above 140 MeV)[1] .

1.3.1 The Giant Resonance

The giant resonance neutrons (GRN) are produced by photons with energies below 30 MeV. The photon transfers its energy to the nucleus by inducing an oscillation in which the protons as a group move in opposite direction to the neutrons as a group. For this process, the cross-section reaches a maximum at photon energies of approximately 20-23 MeV for light nuclei (atomic mass number $A \leq 40$) and 13-18 MeV for medium and heavy nuclei. The GRN process is more important than the other processes because of the large cross-section and the abundance of low energy photons. The average energy of giant resonance neutrons is in the order of a few MeV.

1.3.2 The Pseudo-deuteron Production

For photons with energies between approximately 30 and 300 MeV, the dominant neutron production mechanism is the pseudo-deuteron process. In this mechanism, a high energy photon interacts with a neutron-proton pair within the nucleus, instead of the nucleus as a whole. The pseudo-deuteron cross sections are relatively small, about an order of magnitude below the giant-resonance peak. The quasi-deuteron neutron energies are higher than giant resonance neutron energies, but they are not generally a special problem, due to their substantially lower production rate.

1.3.3 The Photopion Production

Above photon energies of 140 MeV, which is the threshold for photopion production, neutrons can be produced as a result of this reaction. The cross-section goes through a number of resonance peaks. These peaks are only a fraction of the giant resonance cross section, but the neutrons released in this mechanism are higher in energy and much more penetrating than giant resonance neutrons. These neutrons dominate the dose rates

outside shield thicknesses greater than about 2 m of concrete. They also regenerate a field of lower energy neutrons and neutron capture gamma rays due to their reactions with the shielding material.

CHAPTER 2: METHODS OF NEUTRON DETECTION

2.1 INTRODUCTION

In this chapter we will describe the various instruments used for neutron detection in this work, concentrating on the following principles and methods: the Bonner Sphere System (BSS), the rem meter, the moderated BF_3 counter and activation of ^{11}C. Specifics of particular instruments, their calibration and operation will be described in Chapters 3 and 4.

2.2 MULTISPHERE SPECTROMETRY

2.2.1 The Bonner Sphere System (BSS)

Fast neutrons are difficult to detect because of their low interaction cross sections in target materials, typically in the millibarn (10^{-27} cm^{-2}) range. On the other hand, cross sections of a few capture reactions reach thousands of barns for thermal neutrons. Reactions such as $^{6}Li(n,\alpha)^{3}H$, $^{10}B(n,\alpha)^{7}Li$, and $^{3}He(n,p)^{3}H$ are therefore used in very efficient thermal neutron detectors. Consequently, fast neutrons can be detected with more efficiency if they are slowed down to thermal energies. This is best accomplished using a moderating material with a high content of hydrogen, such as polyethylene. Several kinds of neutron detectors, including Bonner spheres [2], are based on the use of a neutron moderator coupled with a thermal neutron detector.

A set of Bonner spheres consists of several polyethylene spherical moderators of different diameters. Originally, the thermal neutron detector used [2] was a LiI scintillator, but ^{3}He proportional counters also became popular in BSS. Spheres of different sizes have different energy responses, as illustrated in figure 2.1. Smaller spheres have the highest

sensitivity to neutrons at relatively low energies. With increasing size, the maximum sensitivity shifts progressively to higher neutron energies, because larger moderator dimensions slow down higher neutron energies. Increasing the moderator size also decreases the sensitivity to low energy neutrons, since these travel only short distances before reaching thermal energies. As a result, they are more likely to be absorbed on hydrogen in the outer layers of a large sphere rather than reaching the thermal neutron detector. Due to their spherical shape, the angular response of Bonner spheres is almost perfectly isotropic.

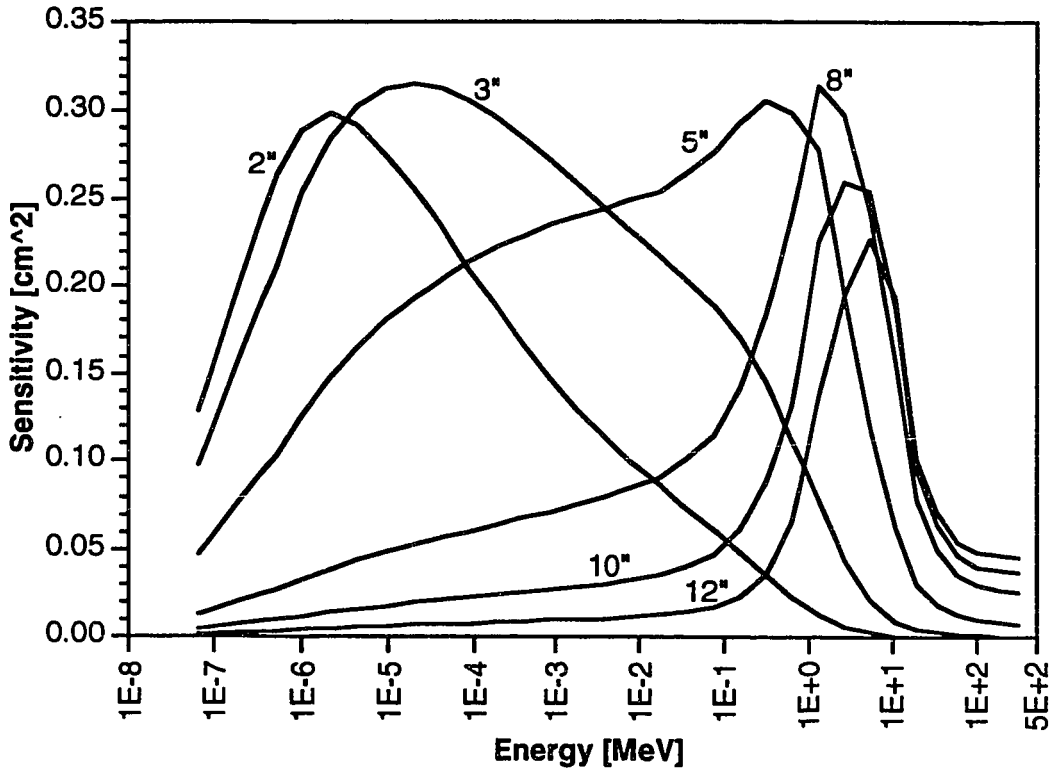

Figure 2.1: Sensitivity of Bonner spheres of various diameters as a function of neutron energy (data calculated by Sanna [14] for a system with a 4 x 4 mm LiI detector).

It can be noted in figure 2.1 that the responses decrease dramatically for the energies greater than roughly 20 or 30 MeV, even for the largest spheres. It is possible, however, to extend the range of the energy response by adding a layer of lead inside the

polyethylene moderator. Since lead has high cross sections for (n,2n), (n,3n), ..., reactions at high neutrons energies, it helps to translate high energy neutrons to lower energy regions, where they are more likely to be detected. This principle was first used by Birattari et al. [3] to increase the energy response of a rem meter (see section 2.4 below).

2.2.2 Unfolding of Neutron Spectra

The fact that spheres of different sizes have different energy responses can be used to determine the energy distribution of the neutron fluence, $\phi(E)$, also called the neutron spectrum. The first step of the procedure consists in performing measurements at a location of interest with every individual sphere. The result is a series of count rates, N_j, where j designates the *j-th* sphere. These count rates can be expressed as:

$$N_j = \int_0^{\infty} S_j(E) \times \phi(E) dE \qquad j=1,2,...,N \qquad (2.1)$$

where $S_j(E)$ is the sensitivity (response) of the *j-th* detector as a function of energy. Solving eq.(2.1) for $\phi(E)$ is called "unfolding" the neutron spectrum. Most practical methods of solving eq. (2.1) approximate the continuous neutron fluence spectrum $\phi(E)$ by a set of constant values ϕ_i in m finite energy intervals or "groups". These energy groups may be a few or numerous, and do not need to be equal. The detector response functions $S(E)$ are similarly approximated by discrete values for the same intervals, creating a response matrix of discrete values, S_{ij}. Response matrices, calculated for a variety of types and dimensions of thermal neutron detectors, are available in the scientific literature. Using this "multigroup" approach, integral equations (2.1) can be replaced by linear equations:

$$N_j = \sum_{i=1}^{m} S_{i,j}\, \phi_i \qquad j=1,2,...,N \qquad (2.2)$$

A number of unfolding programs are available (LOUHI, SAND II, BUNKI,...) to solve eq.(2.2) by numerical methods. In this work, the BUNKI [4] program with the SLAC

response matrix [16] was used. BUNKI is written to be run interactively from the terminal and it gives the user many options such as: choice of the detectors, unfolding algorithm, response matrix, initial spectrum, the number of energy intervals, smoothing, etc. By judicious choice of parameters, the user can direct the program towards solutions that are physically reasonable.

BUNKI calculates the neutron fluence, dose, and dose equivalent as a function of neutron energy. In addition, it also calculates the total fluence, dose, dose equivalent, quality factor, average energy, and responses of selected detectors. A sample input of BUNKI is listed in Appendix A, along with brief explanations of the input data. An output description of BUNKI is provided in Appendix B.

2.3 THE ANDERSON-BRAUN (AB) REM METER

The AB rem meter consists of a cylindrical BF_3 proportional counter surrounded by an inner polyethylene moderator, a boron doped synthetic rubber attenuator, and an outer polyethylene moderator. The synthetic rubber attenuator has a number of holes in the lateral surface and the front and end surfaces. The AB rem meter is designed in this manner so that its energy response is close to the fluence-to-dose equivalent conversion factor curve. In this way, it can be used to measure dose equivalent rate directly using a method explained below.

If the neutron spectrum $\phi(E)$ is known, the dose equivalent can be calculated using equation (2.3):

$$DE = \int_{E_{min}}^{E_{max}} \phi(E)\, h_{\phi}(E)\, dE \qquad (2.3)$$

where $\phi(E)$ is neutron fluence, and $h_{\phi}(E)$ is fluence to dose equivalent conversion factor. The total response (R) of a detector can be expressed as:

$$R = \int_{E_{min}}^{E_{max}} \phi(E)\, S(E)\, dE \qquad (2.4)$$

where $S(E)$ is the sensitivity of the detector as a function of energy. If the $S(E)$ curve has the same shape as $h_\phi(E)$, the latter can be expressed as:

$$h_\phi(E) = \mathrm{k} \cdot S(E) \qquad (2.5)$$

for any E, k being a constant. If eq. (2.5) is true, it follows from (2.3) and (2.4)

$$DE = \mathrm{k} \cdot R \qquad (2.6)$$

that is, the rem meter response is proportional to the dose equivalent, independent of energy and shape of the neutron spectrum. This relationship is to a certain degree, valid from thermal energies to approximately 10 MeV. For higher energies the response drops significantly, because due to its finite size, the polyethylene moderator can no longer moderate high energy neutrons.

2.4 THE LINUS REM METER

Although the performance of the AB rem meter is satisfactory below energy 10 MeV, it can not be used in situations where high energy neutrons are significant. Around particle accelerator facilities, the availability of an instrument with a good sensitivity at higher energies is desirable. Such an instrument was developed by Birattari et al. [3]. It is based on the commercially available SNOOPY rem meter, which is similar to the AB rem meter. This modified rem meter has an additional layer of lead 1 cm thick around the boron plastic attenuator, shifting the polyethylene moderator 1 cm outward, so that its thickness remains unchanged. The lead increases the response in the high energy interval, without significantly affecting the response for lower energies. The enhanced sensitivity in the high energy region is due to the (n,xn) reactions in lead, as mentioned in section 2 of this chapter. In this manner, the response of the modified rem meter was extended up to 400 MeV. This instrument was named "LINUS" by its designers.

2.5 THE MODERATED BF_3 DETECTOR

The moderated BF_3 counter consists of a long BF_3 proportional counter inserted into a cadmium covered cylindrical polyethylene moderator. The BF_3 gas serves both as the target for slow neutron conversion into secondary charged particles and as a proportional gas. The gas is highly enriched in the ^{10}B isotope. Thermal neutrons induce the $^{10}B(n,\alpha)^7Li$ reaction, which has a capture cross section for thermal neutrons of 3840 barns. This makes the BF_3 proportional counter a highly efficient thermal neutron detector. In addition to good detection efficiency, the BF_3 counter is relatively insensitive to γ rays, due to the high energy (Q=2.31 MeV on average) released in the $^{10}B(n,\alpha)^7Li$ reaction. Since the range of the reaction products, an alpha particle and the ^7Li ion, have relatively short ranges in the gas, they will deposit all or most of their energy within the detector medium, giving rise to large pulses from gas ionization. On the other hand, high energy photons will loose only a small fraction of their energy in the counter, and the secondary electrons resulting from photon interactions give rise to much smaller pulses. The response to photons can therefore be eliminated by pulse height discrimination.

The purpose of the Cd layer around the cylindrical polyethylene moderator is to absorb external thermal neutrons incident on the detector. Only neutrons with energy greater than the "cadmium cutoff" (0.4 eV) can enter the moderator. Under optimal conditions, strictly parallel beam incident along its main axis and no scattering from surrounding materials, it could be used to measure the neutron fluence rate independent of neutron energy, because its design is a simplified version of the "long counter" [5]. In this work it is only used to monitor the variations of the neutron field.

2.6 ACTIVATION OF ^{11}C

When neutrons of energy greater than 20 MeV interact with ^{12}C nuclei, ^{11}C is produced by the reaction $^{12}C(n, 2n)^{11}C$. The ^{11}C is a positron emitter with maximum energy 0.98 MeV, and a half life of 20.4 min. The reaction $^{12}C(n, 2n)^{11}C$ can be used with advantage in a plastic scintillator [6], because it contains large amounts of ^{12}C and is a radiation detector in itself. After neutron irradiation, the positrons resulting from ^{11}C activation cause scintillations within the same detector, which can be counted using standard

methods. The cross section as a function of energy of the $^{12}C(n, 2n)^{11}C$ reaction is well known. It has a threshold at ~20 MeV, rises rapidly and becomes flat at ~22 mb for neutrons above 30 MeV. This implies that the scintillator is not sensitive at all below the threshold. Since the scintillator responds only in the high energy region, where the responses of the Bonner spheres start to drop, it is used as a helpful complement to the Bonner spheres. By adding the cross section of the scintillator to the Bonner spheres response matrix, the quality of unfolding neutron spectra for high energy neutrons (> 20 MeV) will be improved.

In the electron accelerator facilities, photons with energy above 20 MeV possibly react with ^{12}C nuclei to produce ^{11}C through the reaction $^{12}C(\gamma, n)^{11}C$. This reaction reaches a maximum at photon energy of ~24 MeV. In order to eliminate this high energy photon interference, the ^{12}C plastic scintillator should be used outside a 2 or 3 feet thick concrete shield where the photon to neutron ratio is not too large. Another way to reduce high energy photon interference is to place a lead brick shielding about 3 cm thick between the detector and the radiation source.

CHAPTER 3: INSTRUMENTATION

3.1 INTRODUCTION

This chapter provides specific information about instrumentation used in this work, such as a description of particular models, associated counting electronics, operating parameters, and other pertinent details.

3.2 BONNER SPHERES SYSTEM

The Bonner spheres system (BSS) at SLAC was purchased from Ludlum Measurements Inc. The thermal neutron detector is a 4 mm x 4 mm enriched Li^6I (Eu) crystal connected to a photomultiplier by a 10 cm long plexiglass light guide. The detector probe in an aluminum housing is the combination of the crystal, light guide, and photomultiplier. It is used together with polyethylene moderating spheres with following diameters: 2", 3", 5", 8", 10", and 12". The density of the polyethylene is 0.955 g/cm^3. A custom 12" Bonner sphere was also ordered from Ludlum Measurements Inc. It contains an additional 1 cm of lead around the polyethylene layer, shifting the polyethylene moderator 1 cm outward in order to preserve the original thickness of polyethylene. The BSS came with a light cart that can be used to support a moderator sphere with the detector probe. This cart has a telescopic column that allows the user to adjust the height of the detector.

The associated counting electronics consist of an Ortec 142 PC preamplifier, Ortec "Nomad" Multichannel Analyzer (MCA), and a lap top computer. The Nomad contains the following built in modules: MCA hardware, amplifier, high voltage supply, and low voltage supply for the pre-amplifier. The lap top computer has the Ortec "Maestro" software used as an interface to the MCA and to store data. The schematic set up of the BSS is shown in figure 3.1. The system was operated with the following parameters: coarse gain 500, fine gain 0.4, and a high voltage 600V.

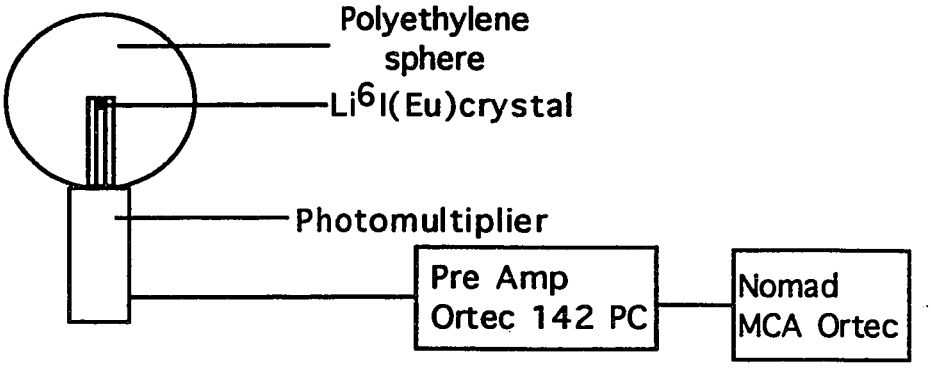

Figure 3.1: Schematic drawing of the Bonner sphere counting system.

A typical MCA pulse spectrum is shown in figure 3.2. The horizontal axis indicates the channel numbers, with 2048 channels being used. The vertical axis shows the number of accumulated pulses in each channel. Pulse height spectra such as the one in figure 3.2 usually exhibit a sharp slope in the lowest channels. This sharp slope is the combination of electronic noise and photons, since the latter produce only small pulses in the detector. In our case, this part of the spectrum was eliminated by raising the MCA discriminator level. Neutron interactions produce large pulses due to high energy (2.31 MeV) released in each (n,α) reaction. These large pulses accumulate into the broad peak at the end of the spectrum. In order to count neutrons only, the ROI, region of interest, is chosen so that it contains only the neutron peak. It can be seen from figure 3.2 that the neutron peak is superimposed on a background continuum. The background can be subtracted by the Maestro software. This introduces a slight uncertainty which adds to the total counting uncertainty.

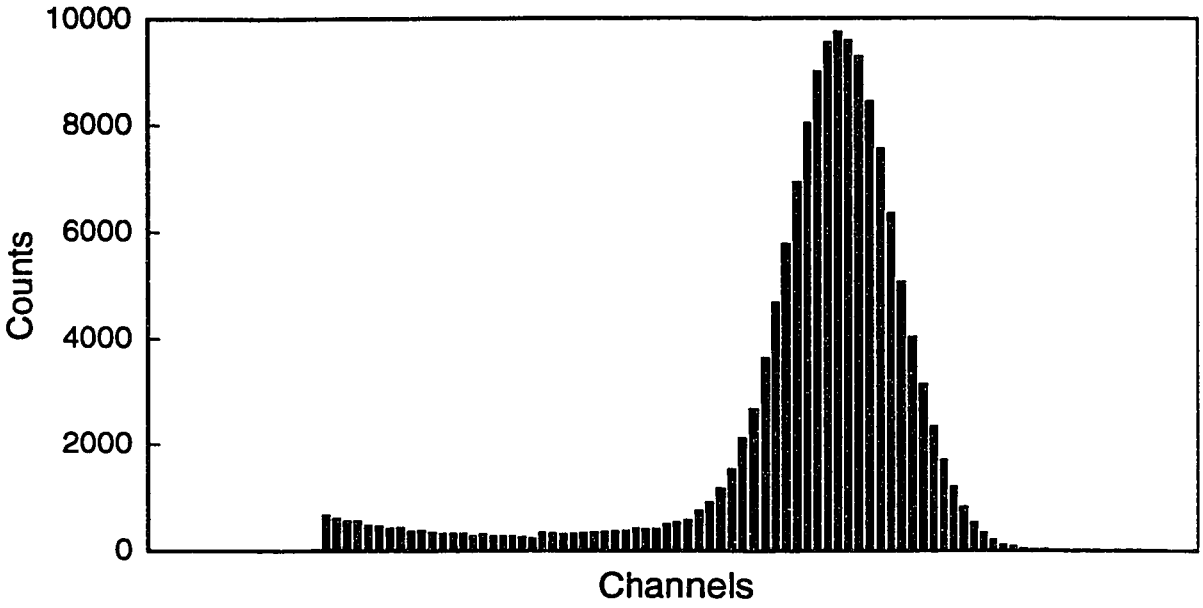

Figure 3.2: This figure illustrates a typical MCA neutron spectrum. The missing lowest part of the spectrum was eliminated using the MCA discriminator.

3.3 ANDERSON-BRAUN (AB) REM METER

The AB rem meter used in this work is similar to the commercially available SNOOPY rem meter. It consists of a cylindrical BF_3 proportional counter of 1.5 cm diameter and 6 cm active length. The gas is enriched to 94% of ^{10}B isotope, and filled to a pressure of 600 mm Hg. This BF_3 is surrounded by:

1) an inner polyethylene moderator;
2) a boron doped synthetic rubber attenuator that has holes on the lateral surface and the front and end surfaces; and
3) an outer polyethylene moderator.

The electronic equipment consists of a pre-amplifier attached close to the counter, and the following NIM modules: high voltage (HV), amplifier (AMP), single channel analyzer (SCA). Figure 3.3 shows the electronic set-up. The AB rem meter was used with the

following parameters: coarse gain 20, fine gain 1.5, and high voltage 1800V. Calibration of the instrument will be described in chapter 5.

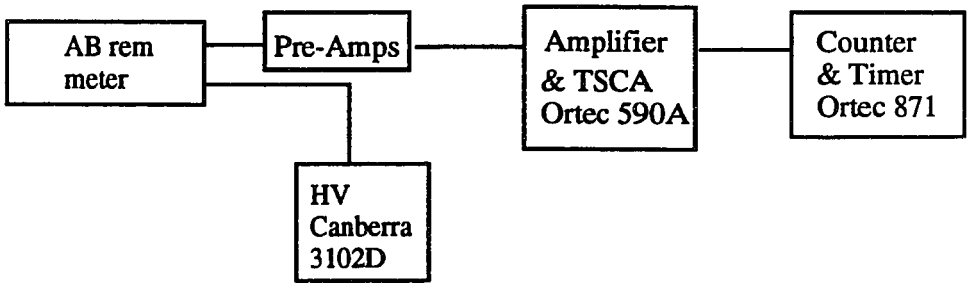

Figure 3.3: Schematic drawing of the Anderson Braun rem meter counting system.

3.4 ANDERSON-BRAUN REM METER WITH LEAD (ABPB)

The rem meter with lead at SLAC is a custom modification of the AB rem meter made by Ludlum following the LINUS design by Birattari et al. [3]. It contains an additional 1 cm of lead around the boron doped synthetic rubber attenuation layer, shifting the polyethylene moderator 1 cm outward in order to preserve the original thickness of polyethylene. The electronic set-up and parameters of this rem meter (ABPB) are the same as described in section 3.3 for the AB rem meter. Both models share the same BF_3 counter.

3.5 MODERATED BF_3 DETECTOR

The moderated BF_3 detector contains a BF_3 proportional counter (Reuter Stokes RS-P1-1613; 5 cm diameter and 33 cm long) surrounded by a cylindrical polyethylene moderator with 6 cm radial thickness and 42.5 cm long, and a layer of cadmium with thickness of 0.08 cm. Figure 3.4 shows the schematic drawing of the electronic set-up of the moderated BF_3. The electronic equipment consists of NIM power supply model 1012H-1 made by B.L. Packer Inc., a linear amplifier model Ortec 590A, and an Ortec 871 counter. The moderated BF_3 detector was used with the following parameters: coarse

gain 54, fine gain 6, and high voltage 2300V. The stability of this detector was checked by reproducibly placing a small Cf source on the top of the BF_3 moderator.

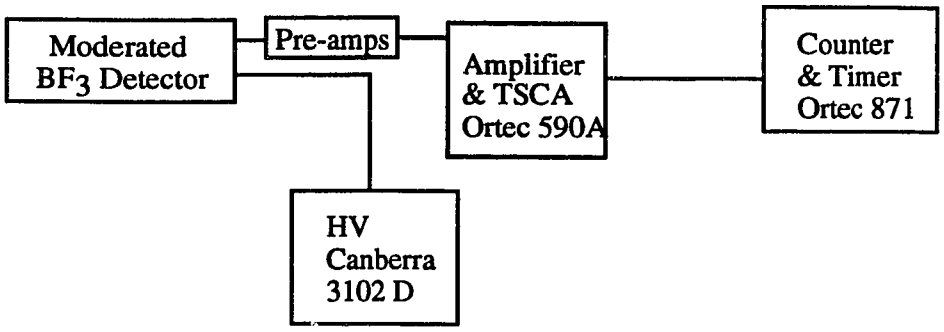

Figure 3.4: Schematic drawing of the moderated BF_3 counting system.

3.6 PLASTIC SCINTILLATOR FOR ^{11}C ACTIVATION

The Radiation Physics group has a number of plastic scintillators. Four of them were used in this work. Each of these scintillators is 5 " in diameter and 5" in high, and weighs 1720 g. All sides, except the bottom, are covered with a reflective layer to increase light collection efficiency. The electronic equipment consist of a 5" photo-multiplier in a shielded cave and a NIM bin with the following NIM modules: high voltage (HV), Amplifier, and a counter. The set up of the plastic scintillator counting system is shown in figure 3.5. The counting system was operated with the following parameters: coarse gain 100, fine gain 1.25, and high voltage 800V. These parameters were determined using a standard source. As indicated in figure 3.5, the lead shielding, covered with black cloth, is used to reduce the background radiation and light. The stability of the system was checked with a ^{60}Co source prior each measurement.

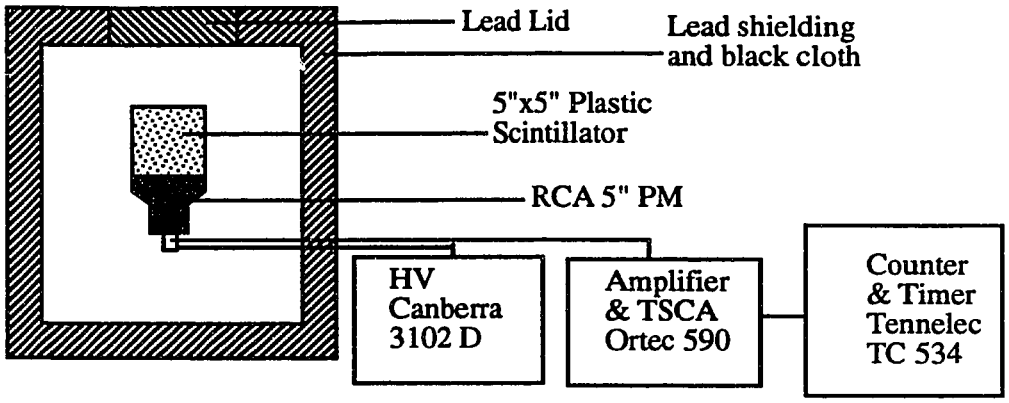

Figure 3.5: Schematic drawing of the plastic scintillator counting system

CHAPTER 4: CALIBRATION OF THE BONNER SPHERE SYSTEM

4.1 INTRODUCTION

The purpose of calibration of the Bonner sphere system (BSS) used in this work is to establish its absolute efficiency, or to determine a constant that will be used to adjust the chosen response matrix to this BSS so that a correct total fluence is obtained in the unfolding procedure. This constant will be a ratio of neutron fluence obtained using the original, uncorrected response matrix to the known direct fluence from the neutron source used in the calibration.

In practical neutron measurements, the BSS responds to both direct neutrons that came directly from a neutron source and scattered neutrons that came from surrounding materials. The contribution of scattered neutrons to the response of the detector can be significant, in some situations the detector's response can be completely dominated by the scattered neutrons. To avoid this situation, the neutron calibration facility ideally should be in a vacuum and free of any neutron scattering surfaces. In practice however, this is not possible. Neutron detector calibrations are typically performed with both the source and the detector at a certain height above the ground. In such a configuration neutrons scattered from the ground and, to a lesser extent, from air molecules, contribute to the detector response. Therefore in calibrating the BSS, a correction for scatter should be performed. Besides scattering, other corrections considered in this work are irradiation geometry and anisotropy of source emission.

Our calibration was done using a ^{252}Cf neutron source. The decay-corrected emission on the date of the experiment was 1.62×10^8 [s^{-1}] (± 3 %). Because the spectrum of this source is well-known, comparing unfolding results obtained with different response matrices enables us to choose the most suitable matrix to be used with this BSS. The best

matrix will be the one that produces a spectrum shape, average energy and fluence-to-dose equivalent conversion factor which are closest to the reference values.

4.2 SCATTER CORRECTION

In the past, various scatter correction methods were devised. These methods usually fall into one of the three categories:

- experimental, such as the shadow cone method [7];
- analytical model for the scattering process; or
- Monte Carlo simulation.

The shadow cone technique consists of placing a cone made of neutron absorbing material between the source and the detector so as to completely block the solid angle subtended by the source and the entry surface of the detector. In this geometry, the detector signal is due only to scattered neutrons, since the direct fluence is absorbed in the cone. A series of two measurements, one with and one without the cone, enable the user to calculate the desired scatter correction. Unfortunately, for a given distance, detectors of different sizes require different shadow cones. For this reason this technique is almost exclusively used only in large and well equipped calibration facilities.

In the analytical approach, a well known model was developed by Eisenhauer [8] and called the "image source model". Jenkins [9] and Sun [10] applied this model as described below. While Jenkins further simplified this model for general use, Sun applied it directly to the particular case of the Bonner spheres. Unlike the analytical methods, derived under various simplifying assumptions, the Monte Carlo method simulates neutron transport in its full complexity. Results of such calculations by Hunter [11] are mentioned below.

To simplify the terminology, in the following text "direct signal" or count rate, fluence, etc. will mean "signal or count rate, fluence, etc. from the unscattered neutrons coming directly from the source". Similarly, "scattered signal" will mean the signal due only to scattered neutrons and "total" will refer to the compounded effect of "direct" and "scattered".

4.2.1 Image Source Model

Eisenhauer [8] has shown that the scattered neutron fluence from a point source at a height h above a ground surface can be described as emitted by a virtual "image" source at a distance h below the ground surface (see figure 4.1). The scattered fluence fraction can be calculated as the ratio of the scattered fluence, $\phi_{scattered}$, to the source fluence, ϕ_{direct}.

$$\frac{\phi_{scattered}}{\phi_{direct}} = \frac{4\alpha h r_o^2}{r_i^3} \tag{4.1}$$

In Equation 4.1, α is the albedo of the reflecting surface, which is defined as the ratio of the reflected neutron fluence to the incident neutron fluence. Albedo data can be obtained from graphs or tables in the literature. In figure 4.1, the distance of the neutron source to the detector is r_o, and r_i is the distance between the image source and the detector. It follows that $r_i^2 = 4\,h^2 + r_o^2$.

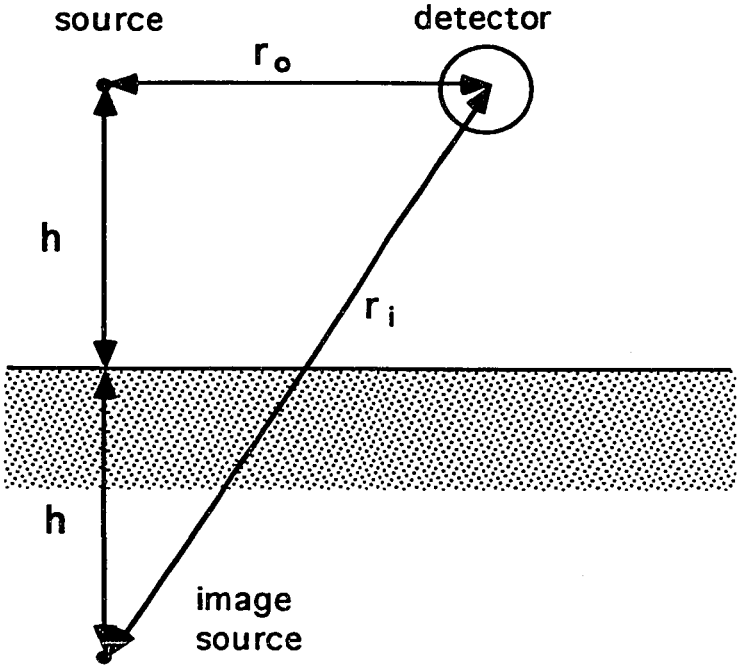

Figure 4.1: Image model geometry. A point source and a detector are separated by a distance r_O at a height h above the ground. An image source is located at a distance 2 h below the point source.

4.2.2 Jenkins' Model

Jenkins [9] developed simple formulae which can be used to calculate ground scattering of neutrons above an earth or concrete surface without relying on albedo data, because these are not always available. These formulae are useful when the normal range of neutron energies used in detector calibration is between 0.2 and 5 MeV. Using the image source model, he found that the dose equivalent (D.E.) and fluence (ϕ) arriving at a detector can be described as:

$$\text{D.E. (Total)} = \frac{QC}{4\pi r_o^2}(1 + f(S)) \tag{4.2}$$

$$\phi\ \text{(Total)} = \frac{Q}{4\pi r_o^2}(1 + f(S)) \tag{4.3}$$

where Q is the source emission; C is the source fluence-to-dose equivalent conversion factor (note that the same C is assumed for direct and scattered neutrons; this is not true in reality), and $f(S)$ represents the scattered fraction of the direct component which is also a function both of r_i and r_o as previously defined. He then used the Monte Carlo code MORSE to calculate fluence and dose equivalent data for a PuBe source. These calculations were done for a wide range of source-to-detector distances and heights above the ground. Plotting the ratio of scattered-to-direct dose equivalents and fluences from MORSE calculations versus r_i/r_o, Jenkins found that the scattered fraction of the direct component can be fitted by the following expressions:

$$f_d = \frac{0.75 r_i / r_o}{(1 + (r_i / r_o)^3)} \tag{4.4}$$

$$f_f = \frac{1.26 r_i / r_o}{(1 + (r_i / r_o)^3)} \tag{4.5}$$

where f_d is the ratio of scattered dose equivalent to direct dose equivalent and f_f scattered fluence to direct fluence. These simple fluence and dose equivalent formulae produced an error of less than 10% when they were checked against measurements with a PuBe source.

4.2.3 Rai-Ko Sun's Model

Sun measured count rates as a function of distance from a planar concrete floor with a set of eight Bonner sphere detectors and four isotopic neutron sources, ^{238}PuBe, ^{238}PuLi, ^{238}PuB, and ^{238}PuF. He used these data to determine the contributions of scattered neutrons to the response of the detectors using the "image" source model. From the calculations, he concluded that the ratio of the total measured response to the response A_d of the unscattered "direct" neutrons for each sphere size at different values of r_o/r_i can be expressed as:

$$\frac{A_t}{A_d} = 1 + \frac{\varepsilon_i}{\varepsilon_o} \times \left(\frac{r_o}{r_i}\right)^2 \tag{4.8}$$

where A_t is the total measured response to both scattered and unscattered neutrons. ε_o is the emission of the source, and ε_i is the emission of the image source. r_o and r_i are as previously defined. In his analysis, he assumed ε_i to be a free parameter that depends on the detector size. For each particular detector, experimental data were fitted with equation (4.8) to determine the ratio $\varepsilon_i/\varepsilon_o$. Dependence on energy or source type was neglected. Actually, any potential energy dependence might have been discarded during data analysis, because every data set for a given sphere and given source was individually adjusted so as to fit a single curve for one sphere and all four sources combined.

In the next step, by regression of the above results for all spheres, he found the relationship between $\varepsilon_i/\varepsilon_o$ and sphere diameter, d, as:

$$d = 4.83 + 7.12 \times \left(\frac{\varepsilon_o}{\varepsilon_i}\right)^2 \tag{4.9}$$

By substituting equation (4.9) into (4.8), the ratio of the total measured response to direct response can be rewritten as:

$$\frac{A_t}{A_d} = 1 + \left[\frac{2.67}{\sqrt{d - 4.83}} \times \left(\frac{r_o}{r_i} \right)^2 \right] \qquad (4.10)$$

The second term in eq.(4.10) is the ratio of counts from scattered neutrons to direct neutrons for each sphere.

4.2.4 Hunter's Calculations of Scattered Neutrons

Hunter [15] used the Monte Carlo code MORSE to calculate the spectra and relative fluence of scattered neutrons in various geometries, including scattering from a plane ground and an enclosed room. In addition, he also calculated the response to the scattered neutrons for several common neutron detectors. In this work, only the spectra of ground scattered neutrons are used. For ground scattering, Hunter found that the scattered fluence calculated by MORSE agreed with the image model and Jenkin's model within 5% only if applied within $r_O \leq h$, otherwise within 15%.

4.3 CORRECTION FOR IRRADIATION GEOMETRY

When a detector is irradiated by a point source, it is generally assumed that the detector response is proportional to the fluence, i.e. it varies as $1/D^2$, where D is the detector-source separation distance. For a spherical detector, the separation distance is measured from the center of the sphere. The above assumption implies that the dimensions of the detector are negligible in comparison with the separation distance D. In this case, the neutrons impinge on the detector in a geometry which is very close to that of a parallel beam. The total number of neutrons impinging on the detector can be then calculated as a product of the fluence at a given point, in the absence of the detector, times the cross-sectional area of the detector presented to the beam.

If a spherical detector of radius R is placed in the field of a point source at a distance D, where the ratio R/D is not small enough, the detector response will no longer vary as $1/D^2$. It will be proportional, in first approximation, to the number of neutrons impinging

on the sphere, determined by the solid angle subtended by the point source and the sphere (see fig.4.2).

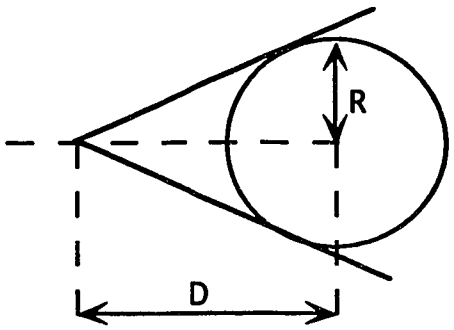

Figure 4.2: Neutrons from a point source striking a sphere of radius R; D is distance between source and detector.

It can be shown from geometrical considerations that this number will always be higher than the same number calculated for a parallel beam geometry, assuming the same fluence at the center of the detector. In reality, this response increase is somewhat lower than predicted from geometrical arguments. This is due to the fact that the mean path of a neutron through the sphere is shorter in the divergent beam than in the parallel beam, which results in a loss of detection efficiency.

Response functions of Bonner spheres are usually calculated for an isotropic neutron field, which is, in a strictly spherical geometry, equivalent to a parallel beam. A correction is therefore needed if calibration measurements are performed very close to the source. Vylet [12] has calculated these correction factors as a function of neutron energy, sphere radius and the R/D ratio. He found that a correction should be applied when the ratio of $R/D \geq 0.2$; for $R/D < 0.2$, the correction becomes negligible.

Using the above criterion, the correction was necessary only for a 12" sphere at distances of 51.5 cm and 77 cm. The corresponding correction factors for neutrons with energy of 2 MeV are 1.013 and 1.006 [12]. The count rates of the 12" sphere at these two distances are corrected using equation (4.11):

$$N_F = N_R / CG \tag{4.11}$$

where N_R is the measured number of count rates, CG is the above correction factor, and N_F is the number of count rates after correction.

4.4 ANISOTROPY CORRECTION OF THE ^{252}CF SOURCE

The ^{252}Cf neutron source used in this study was calibrated by Savannah River Laboratory against a NIST-calibrated ^{252}Cf source [13]. The original cylindrical source with dimensions 1cm x 1cm was further encapsulated at SLAC in an aluminum container of 2.54 cm in diameter and 8 cm in length. Since there was no documentation available indicating the exact position of the source in the cylindrical container, we performed an autoradiograph by simply positioning the source over a sheet of Polaroid film and leaving it there for an exposure of ten minutes. The resulting image was then scanned and enhanced using Adobe Photoshop software. By collapsing the optical density spectrum into seven discrete intervals, it was possible to locate the position of the source in a fairly accurate manner, as illustrated in figure 4.3.

The presence of the aluminum holder modifies the emission of neutrons into a particular solid angle, due to both attenuation and scatter in the holder. To account for this effect, a correction "anisotropy" factor is applied to the fluence calculated at a given distance based only on the source emission. In our calibration measurements our detectors were located in the direction perpendicular to the main axis of the cylindrical aluminum capsule. In this direction, according to Liu et al.[13], the anisotropy factor is 1.1. The 10% increase is due to the scatter in the holder, which is not offset by attenuation through the thin layer of aluminum. This effect is illustrated in figure 4.4: to the direct neutrons (b) emitted in the desired direction, added contribution comes from scattered neutrons (a) and (c).

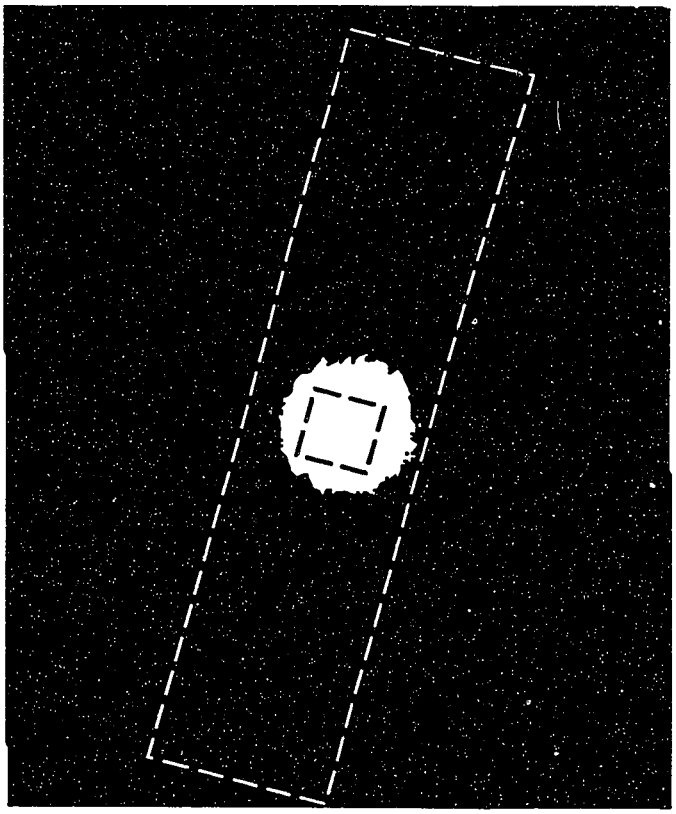

Figure 4.3: Polaroid autoradiograph used to determine the location of the ^{252}Cf neutron source. The dashed outlines indicate the aluminum holder and the Cf source in its center.

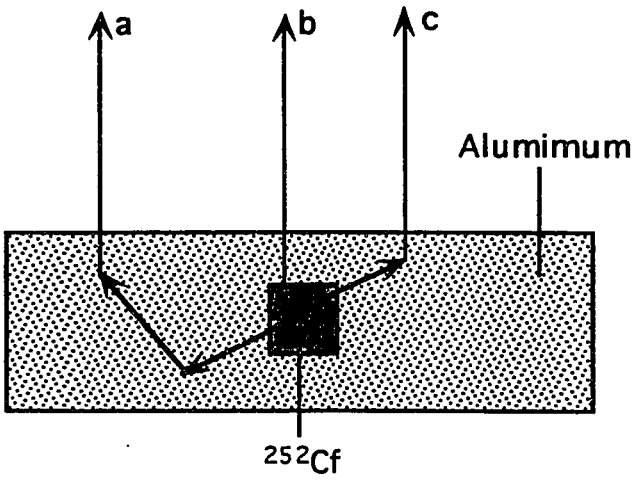

Figure 4.4: This illustrates a ^{252}Cf source and its cylindrical aluminum holder. It also shows scattered neutrons in aluminum.

4.5 CALIBRATION MEASUREMENTS

Calibration measurements were carried out at the hazardous waste yard. This location is an open space covered with a plane concrete floor. It has a thin metallic roof supported by a few iron columns that are approximately 6 m in height. Because the roof is so high, the contribution of scattered neutrons from the roof is insignificant. This geometry is therefore very close to that considered in the scatter correction methods discussed in 4.2. Measurements were made with each sphere at seven different distances from the source: 51.5, 75, 100, 130, 160, 200, and 250 cm. This enabled us to perform a statistical regression using the image model for scatter correction in order to determine necessary parameters. The height of the source and detectors above the concrete was 150 cm. At least 10,000 counts were acquired with each sphere in order to keep the statistical uncertainty below 1%. Data were grouped according to the diameter of the spheres, each group containing results from seven different distances.

4.6 DATA ANALYSIS

This section describes calculations of the scatter correction of measured data using two models described in section 4.2, Rai-Ko Sun and regression based on the image model. Jenkins' model and Hunter's calculation for scattered neutrons do not use measured data. The results from these models will be shown in section 4.6.3 in comparison with the other two models.

4.6.1 Image Model

Based on the image model, the total counts of each sphere at a given source-detector distance can be expressed as:

$$N = \frac{s\varepsilon}{4\pi r_o^2} + \frac{s'\varepsilon'}{4\pi r_i^2} \tag{4.12}$$

where N is the total count rate of a sphere, ε is the direct neutron emission, s is the sensitivity of this sphere to direct neutrons, ε' is defined as scattered neutron emission, s' is the sensitivity of detector to scattered neutrons and r_o, r_i as defined previously. By setting $A = s\varepsilon/4\pi$, and $B = s'\varepsilon'/4\pi$, equation (4.12) can be rewritten as:

$$N = \frac{A}{r_o^2} + \frac{B}{r_i^2} \tag{4.12A}$$

and A and B can be determined by regression analysis, using the measured count rates N and known r_0 and r_i values.

Regression was performed using Delta Graph (version 2.0.3 b) software for Macintosh. Substituting A and B back into eq.(4.12A) and knowing the total counts from measurements at given distances, signal counts due to scatter were determined. The percentages of scatter contribution to direct neutron signal at various distances are presented in Table 4.1.

Two important trends were expected in Table 4.1. First, for a given sphere, the scatter contribution should increase with distance. Second, the scatter contribution should decrease with an increasing sphere radius at a given distance, because larger spheres are less sensitive to softer scattered neutrons. Based on the above assumption, the scatter contributions of the 5" and 10" spheres for all locations did not follow the second criterion. We believe that this is due to the high sensitivity of the fitting procedure to small imperfections in the measured data. Since the scatter contribution seemed to follow a clear pattern for all the other spheres, the scatter contributions of the 5" and 10" spheres for all locations were estimated by interpolation as explained below.

The percentages of scatter contribution at a given source-to-detector distance were plotted against diameters of the Bonner spheres on a log-log scale, as illustrated in figure 4.5, for the distance of 200 cm. It can be clearly seen that, if we exclude the 5 and 10" spheres, all the other square points lie on a slightly curved smooth line, following a trend expected from physical arguments. With respect to this curve, the round points representing the 5" and 10" sphere are obvious outliers. This pattern is repeated in quite similar manner at all other distances. The percentages of scatter contribution for the 5" and 10" spheres were therefore estimated by interpolation at all available distances. Interpolated results are shown in Table 4.2.

Once the percentages of the scattered Bonner sphere signal at given distances were established, the direct count rates were calculated. The direct fluence rates were obtained by unfolding the direct count rates at each distance using the BUNKI program. The total fluence rates were also calculated by unfolding the total count rates, N, that contain both direct and scattered neutron signals. From the direct and total fluence rates obtained by unfolding, the scattered fluence rates were also calculated by simple subtraction. The above results for different distances are shown in Table 4.3.

Table 4.1

The percentages of scatter contribution to the direct neutron signal at various distances calculated using the image model.

d (cm)	2"	3"	5"	8"	10"	12"
51	19.5	7.2	8.2	2.1	N/A	1.4
75	42.9	14.4	14.2	4.0	1.2	2.9
100	65.4	25.2	27.3	7.2	2.1	5.1
130	98.2	38.6	45.4	11.4	3.2	7.9
160	144.9	55.8	70.5	16.4	4.5	10.9
200	221.7	82.8	129.3	23.1	6.1	15.3
250	447.4	120.5	216.3	30.9	8.0	20.4

Table 4.2

The estimated percentages of the scatter contribution to the signal of 5" and a 10" spheres at different distances.

d (cm)	51	75	100	130	160	200	250
5"	4.4	8.9	12.9	19.8	33.7	48.9	73.9
10"	1.6	3.3	4.1	6.3	12.8	17.9	23.9

Table 4.3

Direct and total fluences, and the fraction of the scattered fluence to direct fluence for different distances, based on the image model.

d [cm]	ϕ_d [n/cm^2]	ϕ_{Total}[n/cm^2]	ϕ_S/ϕ_d [%]
51	1.2×10^7	1.2×10^7	3.4
75	5.5×10^6	5.9×10^6	9.2
100	3.1×10^6	3.4×10^6	12.2
130	1.9×10^6	2.2×10^6	17.9
160	1.2×10^6	1.5×10^6	24.9
200	7.5×10^5	1.0×10^6	35.5
250	4.5×10^5	6.9×10^5	52.6

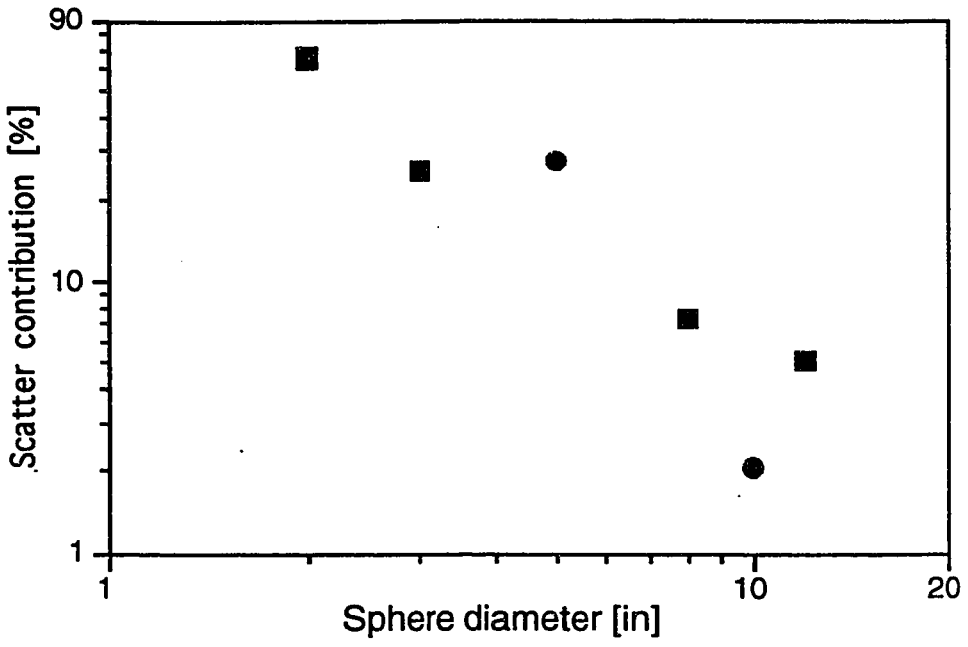

Figure 4.5: Relation between the scatter contribution and sphere diameters for the source to detector distance of 200 cm. The round points represent 5" and 10" spheres. The square points represent 2", 3", 8", and 12" spheres.

4.6.2 Jenkins' s Model

Scattered fluence fractions *(ff)* were calculated using eq.(4.5) for distances used in our calibration measurements. These fractions are shown in Table 4.4.

4.6.3 Rai-Ko Sun' s Model

The ratio of the scattered neutron response to the direct response for each sphere was calculated using the second term in eq.(4.10) for the distances used in our calibration measurements. Using the ratios, scattered neutron signals were calculated for each sphere at a given distance. From the measured total signals and scattered neutron signals, the

direct neutron signals were obtained by subtraction. The direct and scattered neutron signals were then unfolded using the BUNKI program to obtain direct and scattered fluences, from which the fraction of scattered to direct fluences was calculated. These fractions are presented in Table 4.4.

4.6.4 Hunter's Calculations

We were able to obtain from Hunter [11] the calculated scattered spectra, normalized to an emission of one neutron, tabulated as fluence per unit lethargy in the multigroup structure used by the BUNKI program [4]. These spectra were calculated with the distances between the source and detector at 50, 75, 100, and 200 cm, and at a height of 150 cm above the ground surface. From a scattered spectrum, the total fluence of scattered neutrons, ϕ_{ts}, was calculated using the following equation:

$$\phi_{ts} = \sum_{x=1}^{N} \phi_{ux} \times \log \frac{E_{x+1}}{E_x} \tag{4.13}$$

where ϕ_{ux} is fluence per unit lethargy in group x, where E_x and E_{x+1} are the limits of the energy interval defining the group x. The direct neutron spectrum of a ^{252}Cf source was also obtained from Hunter and normalized to an emission of one neutron. The direct fluence was calculated by multiplication of the neutron emission by $(1/4\pi r^2)$, where r is the distance from the source. With the above information, the fraction of the scattered fluence relative to the direct fluence at different distances was calculated. These results are presented in Table 4.4

4.6.5 Comparison of Different Models

The scattered fluence fractions predicted, directly or indirectly, or using unfolding by various models, are listed in Table 4.4 and plotted in figure 4.7. Results from Sun's model are in most cases lower than the other models. There does not seem to be any other systematic trend. Results from the image model show good agreement with Jenkins'

model and Hunter's calculation for some distances. However, the scatter contribution of the image model at the distance of 250 cm is 30% higher compared to all other models.

Table 4.4

Percentages of scattered neutron fluence relative to direct fluence for various models at different distances.

Distance [cm]	Image model [%]	Jenkins's model [%]	Hunter's calculation [%]	Sun 's model [%]
51	3.4	3.6	4.5	3.5
75	9.2	7.3	8.7	7.4
100	12.2	12.2	13.8	11.1
130	17.9	18.7	N/A	16.0
160	24.9	25.3	N/A	22.2
200	35.5	33.1	36.8	30.8
250	52.6	40.2	N/A	40.4

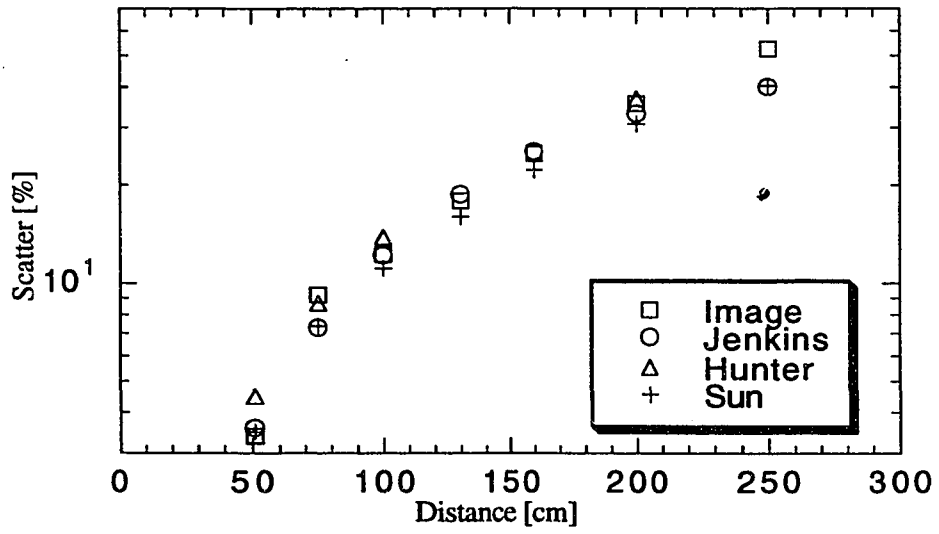

Figure 4.6: Scatter contribution as a function of distance for different models.

4.6.6 Calibration Factor and Response Matrix

The scatter contributions obtained from various models for different distances do not differ dramatically, as illustrated in figure 4.6. Results from any of these models could be used to perform the scatter correction. The image model was selected for this purpose, because it was the only model that made explicit use of our experimental data measured at different distances. After the scatter correction, the direct count rates were unfolded using the BUNKI program with Sanna's matrix to obtain direct fluences. This matrix was chosen because it gave the most accurate neutron spectrum and the average energy for the ^{252}Cf.

The calibration factor used here, as described in section 4.1, is the ratio of the neutron fluence obtained using the original, uncorrected Sanna's response matrix, to the known direct fluence from the neutron source used in the calibration. The fluence rate at a distance of 100 cm from the ^{252}Cf neutron source was chosen to calculate the BSS calibration factor using equation (4.14):

$$\phi_o = \frac{\varepsilon F}{4\pi r^2} \tag{4.14}$$

where ε is neutron emission rate, F is the anisotropic factor mentioned earlier, and r is the detector-to-source distance. This reference value is ϕ_o=5.16x10^6 neutrons/cm^2. The fluence rate obtained from unfolding detector data is equal to 3.052x10^6 neutrons/cm^2. The calibration factor is therefore equal to 0.59. This means that our detector system, with the electronic setup and ROI selection scheme as described in chapter 3, has a lower sensitivity by a factor of 0.59 compared to Sanna's matrix.

Sanna's response matrix contains only response functions for standard polyethylene spheres. In order to be able to include the data from the 12" sphere with lead and the ^{11}C scintillator in the unfolding process, a new matrix, called "SLAC", was generated by Vylet [16] in the following manner:

- Sanna's matrix for the 4x4 mm LiI was multiplied by the above calibration factor.

- response function for the 12" sphere with lead, together with ordinary 12" and 10" spheres, was calculated using the LAHET and MCNP codes. Responses for the standard spheres were used to find the adjustment factor used to integrate the 12" sphere with lead to the modified Sanna's matrix.
- The cross section for the reaction $^{12}C(n, 2n)^{11}C$, multiplied by the total number of atoms in the 5"x5" plastic scintillator, was added to the above matrix. Saturated activity of the scintillator can be then treated as sphere count rate in the BUNKI input.

A modified version of the BUNKI code was developed to reflect the above changes.

CHAPTER 5: CALIBRATION OF THE REM METERS AND ^{11}C ACTIVATION SYSTEM

5.1 CALIBRATION OF THE ^{11}C ACTIVATION SYSTEM

The counting set up for the plastic scintillator is a so called 4π counting system. It has the ability to detect all scintillations occurring within the scintillator regardless of their position or the direction of the emitted positron. As a results, this system should detect 100% of scintillations with the discriminator level set to zero. However, in practice it is impossible to count the ^{11}C activity at this level, because of the large number of small pulses from the background and electronic noise. To overcome this problem, a sufficiently high discriminator level needs to be applied. At this level, the ratio of signal from the ^{11}C activity to the background noise should be at least 2 to 1. The optimum discriminator level was determined during the calibration process.

Every plastic scintillator was kept in a plastic bag to prevent contamination during irradiation. It was brought to the neutron field Final Focus Test Beam (FFTB) and exposed up to 40 minutes. It was then brought back to the counting lab located in Bdg 3 at SLAC. The exposed scintillator was counted for 100 sec to 5 mins at different discriminator levels. The low discriminator (LLD) level was varied from 0.5 to 6 V in 0.5 V steps. The upper discriminator level (ULD) was used only at two values: 5 V and 10 V. After the counting was finished, the plastic scintillator was let to decay for more than ten half lives or overnight before counting its background. The time needed to count the background was 20 minutes. It was counted at the same low and upper discriminator levels mentioned above. The same approach was repeated with several different plastic scintillators.

5.1.1 Determination of the Optimal Discriminator Level

It is unavoidable that the scintillator counting occurs with a certain delay after the end of irradiation, while the ^{11}C activity is decaying. For each of the different discriminator settings above, the activities at the end of irradiation, A_{irr}, were calculated using the following equation:

$$A_{irr} = \frac{C\lambda}{e^{-\lambda t_d} - e^{-\lambda(t_d + t_c)}} \tag{5.1}$$

where C is the net count rate defined as the difference between the gross and background count rates. The decay constant λ has a value of 0.034 min^{-1}, and t_C is the counting period in minutes. The decay time t_d is a period of time between the end of irradiation and the start of counting. For each given discriminator level, the A_{irr} value was compared to the background measured at the same discriminator level. Comparing these values, we found that the discriminator levels of LLD=0.5V and ULD=5V provide the best ratio of signal to noise.

5.1.2 Calculation of the Efficiency

Because the discriminator window of 0.5V to 5V was selected, it was necessary to determine the efficiency of the counting system at this discriminator level. First, count rates were plotted as a function of the lower discriminator level (see figure 5.1). An integral bias curve was drawn through these points, and extrapolated to zero discriminator level. The efficiency was calculated as the ratio of count rates at LLD=0.5V to the extrapolated rates at LLD=0.0V. The same approach was repeated for two other scintillators. The average efficiency was determined as 91% ± 3%. This efficiency was applied in calculations of saturated activities mentioned in the next section.

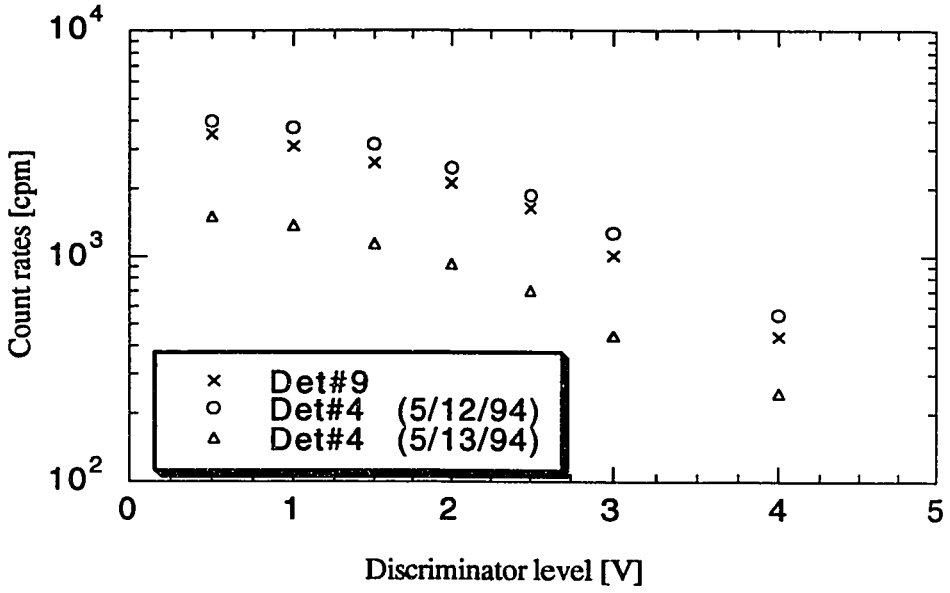

Figure 5.1: Counts rate versus discriminator levels for three different plastic scintillators.

5.1.3 Calculation of Saturated Activity

For a scintillator exposed in a neutron field, the saturated activity, i.e. activity obtained for an infinite irradiation period at a given fluence rate, can be calculated using the following equation:

$$A_{sat} = \frac{A_{irr}}{(1 - e^{-\lambda t_{irr}})\varepsilon} \tag{5.2}$$

where A_{irr} is the activity at the end of irradiation that can be obtained using eq.(5.1), λ is the decay constant defined previously, t_{irr} is the time used to irradiate the scintillator and ε is the counting efficiency at the chosen discriminator level.

5.2 CALIBRATION OF THE AB AND ABPB REM METERS

Rem meter calibration measurements were performed outside the low level waste yard, in an open space with a flat paved ground. The Cf source was placed at the distance of 2.26 m above the ground, and the distance of rem meter above the ground was at 2.16 m. The distance between the Cf source and rem meter was 1 meter. At this height and relatively short source-to-detector distance, the scatter contribution is low, below 3%. This was estimated using Rai-Ko Sun's model for a 10" sphere, because AB rem meter has the same thickness of polyethylene as a 10" sphere. Measurements were carried out for both types of rem meter. Data were collected long enough to keep the statistical uncertainty below 1%.

The calibration factor expressed in units [rem/count] for each rem meter was calculated using the following equation:

$$c = \frac{h_\phi \cdot \varepsilon \cdot F \cdot t}{4\pi d^2 N} \tag{5.3}$$

where h_ϕ is the fluence to dose equivalent conversion factor (rem cm^2) for ^{252}Cf obtained from Liu et al [13]. ε is the source emission, and F is the anisotropy correction factor defined previously. d is the distance from source to detector, t is the irradiation time, and N is the number of counts collected. The resulting calibration factors were 1.088 $x10^{-7}$ rem/count for the AB and 1.107 $x10^{-7}$ rem/count for the ABPB rem meter.

CHAPTER 6: MEASUREMENTS

6.1 INTRODUCTION

It was possible to perform measurements at SLAC facilities only when the beam was available and the machines were being used under certain specific conditions. Scheduling of our measurements was therefore totally dependent on the experimental program of the facilities involved. As a result, the measurements were performed in the following sequence:

Location	Date
FFTB	5/12/94 - 5/15/94
SSRL-booster	08/02/94 -08/04/94
SSRL-Linac	08/10/94 -08/14/94
SSRL-Linac diagnostic room	03/27/95-03/30/95

6.2 FINAL FOCUS TEST BEAM (FFTB)

The Final Focus Test Beam (FFTB) is a new beamline at SLAC. The purpose of this facility is to focus the electron beam to an extremely small size as a part of on going research for the Next Linear Collider (NLC) project. The 50 GeV electron beam injected in the FFTB is produced in the SLAC two-mile-long linear accelerator. Neutron measurements at FFTB were performed at three different locations outside the FFTB beam dump (see figure 6.1). Location 1 was on the side of the beam line (FFTB-side) at 90 degrees with respect to the dump. Location 2 was on the ground close to the shielding wall, in the forward direction with respect to the beam. It was found during preliminary surveys that this was the location with the highest dose rates (FFTB-hot spot). At the

location 3, detectors were placed on a wooden box (FFTB-wood), the same height as the beam line.

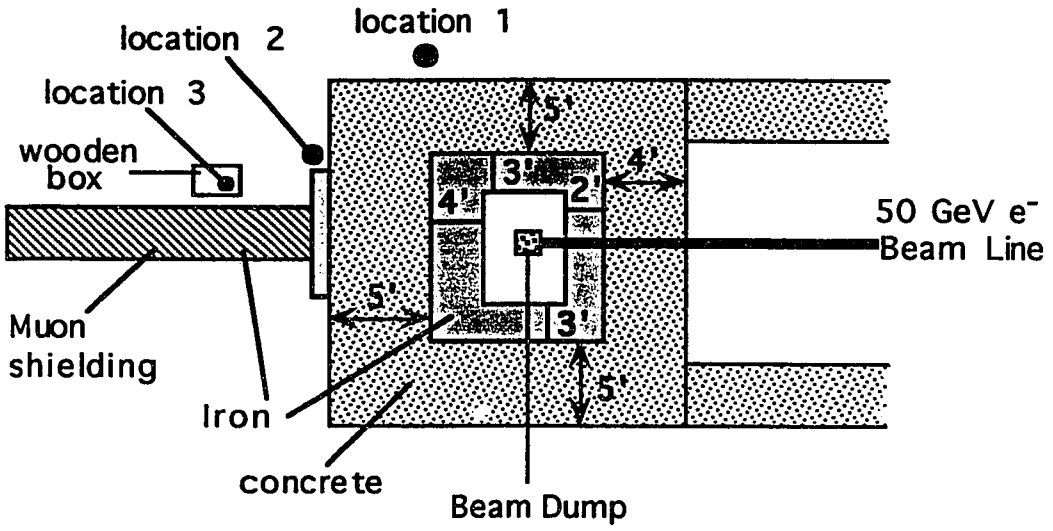

Figure 6.1: Neutron measurements at three different locations outside FFTB dump.

6.3 STANFORD SYNCHROTRON RADIATION LABORATORY (SSRL)

The SSRL consists of a 120 MeV linac, a 3 GeV booster-synchrotron, and storage ring. Neutron measurements at SSRL were performed at different locations: two at SSRL booster-synchrotron, at 90 and 45 degrees with respect to the beamline, and two at SSRL Linac, on the roof above the faraday cup and inside the diagnostic room.

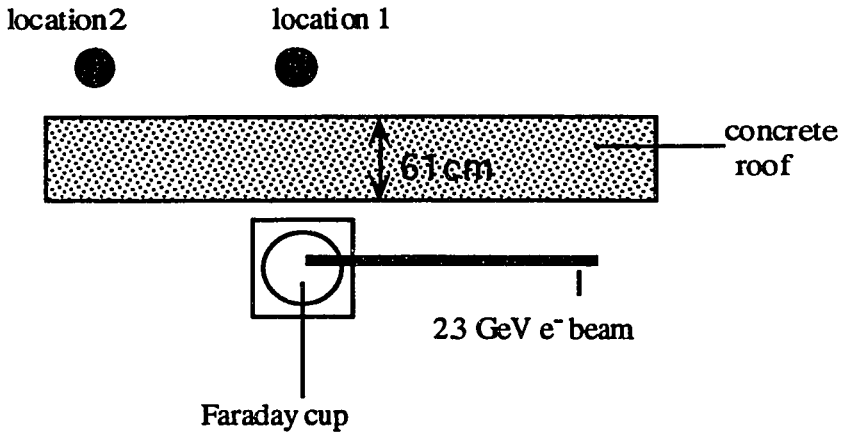

Figure 6.2: Measurements at Booster-Synchrotron SSRL above a faraday cup - Vertical view.

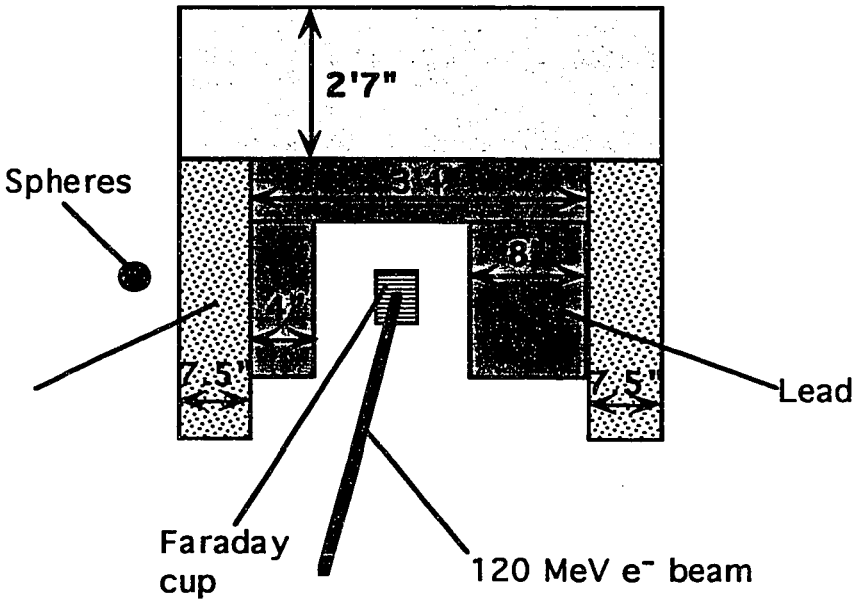

Figure 6.3: Vertical view at SSRL Linac - diagnostic room.

CHAPTER 7: RESULTS

7.1 DATA ANALYSIS

Neutron spectra measurements using Bonner spheres system were always carried out one sphere at a time. Because the beam intensity can fluctuate in time, a reference monitor was used in all measurements. In most cases, the monitor was a BF_3 counter, with exception of the SSRL-linac diagnostic room, where a rem counter was used. At a given location, sphere count rates were normalized to a selected count rate of the reference monitor. The normalized count rates were then expressed in counts per hour, so that their use in BUNKI provides directly dose equivalent in rem per hour. With the same approach, ^{11}C saturation activities were also normalized to the monitor, and expressed in disintegrations per hour. The rem meter data were normalized in the same way. Unfortunately, due to the gain fluctuations of the counting system while counting scintillators exposed at the SSRL-booster, the ^{11}C data were not used in the unfolding. On the roof of the SSRL-linac, data obtained from measurements using Bonner spheres and ^{11}C activation could not be used because of low counting statistics.

Because all electron accelerators at SLAC are pulsed machines, the issue of dead time needs to be addressed. For example, during the measurements at FFTB the electron beam was delivered in short pulses (duration of 30 ps) at a rate of 30 Hz. It is clear that our detectors could not handle even very low count rates, if the neutrons arrived in such short bursts. Fortunately, for detectors based on neutron moderation, it was observed [17][18] that the process of neutron moderation has the effect of considerably spreading the arrival of neutrons in time, typically over several hundreds of microseconds. Considering that the dead time for a NIM electronic setup is on the order of 2 μs, measurements of neutrons generated from short electron bursts become possible. As mentioned above, in most of our measurements very long acquisition times were needed to achieve a reasonable statistical uncertainty. The dead time correction would be most needed for the reference moderated BF_3 counter, because it was by far the most sensitive. However,

since typical BF_3 count rates were on the order of 50 counts/s, no dead time correction was performed.

7.2 UNFOLDED NEUTRON SPECTRA

Unfolding of neutron spectra is a complicated mathematical procedure, requiring experience and judgment. It is therefore useful to solicit advice of an expert in the use of unfolding code and spectra interpretation. Additional insight can be gained by experimenting with unfolding neutron spectra repeatedly with varying parameters. These are, for example, the initial guess spectrum, number of iterations, and using the smoothing parameter. Using all the above, the following approach was adopted:

- The initial spectrum used is constant over most of the energy range, with exception of the last three energy groups, where it gradually decreases. Since the neutron spectra are totally unknown, using the flat initial spectrum prevents any spectrum bias. Measured and calculated spectra behind thick shielding at CERN indicate a decreasing trend at the high energy end. Based on this knowledge, the initial spectrum used was also given this shape at its end.
- In general, no more than 30 to 100 iterations were used. This number of iterations was sufficient to reach a reasonable agreement in BUNKI between the measured and calculated sphere count rates, where the calculated rates were obtained using the unfolded spectrum and the sphere response functions. Performing a greater number of iterations would further improve the agreement between measured and calculated responses, but this tends to create artificial features such as peaks and slopes in the neutron spectrum. This usually means that we are trying to obtain a result which is more accurate than our input data.
- Smoothing was not needed in the unfolding, since spectra obtained with the low number of iterations above were still relatively smooth.

An sample BUNKI input file is listed in Appendix A. At the end of the unfolding procedure, BUNKI writes out two different files: an output file and an input file for the graphics program TOPDRAW, containing the neutron spectrum. The output file contains information such as total fluence, fluence in each energy group, average energy, dose equivalent, and other pertinent data. A sample of BUNKI output is listed in Appendix B.

Neutron spectra for all locations are shown in figure 7.1-7.6. They are plotted in the common form of fluence per unit lethargy. Other unfolding results are summarized in table 7.1, in comparison with the rem meter results.

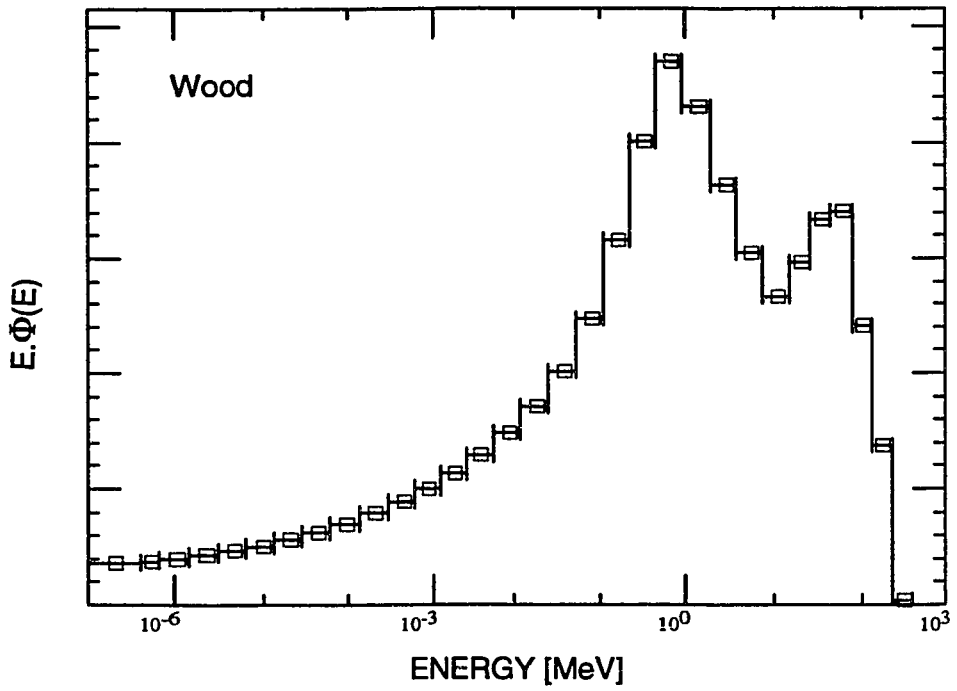

Figure 7.1: Neutron spectrum for FFTB-location 3 (wooden box).

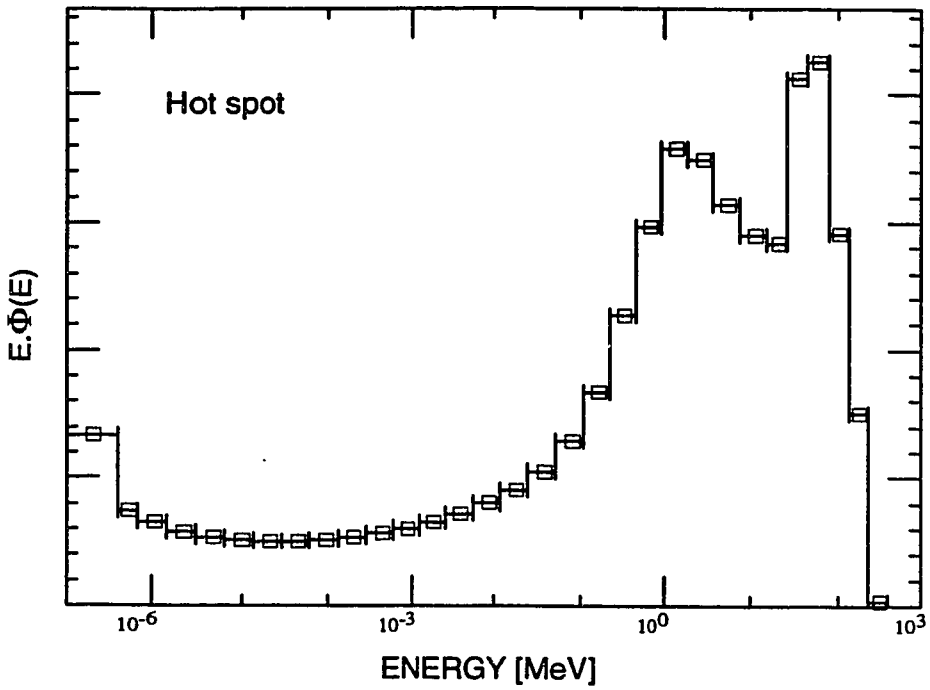

Figure 7.2: Neutron spectrum for FFTB-location 2 (hot spot).

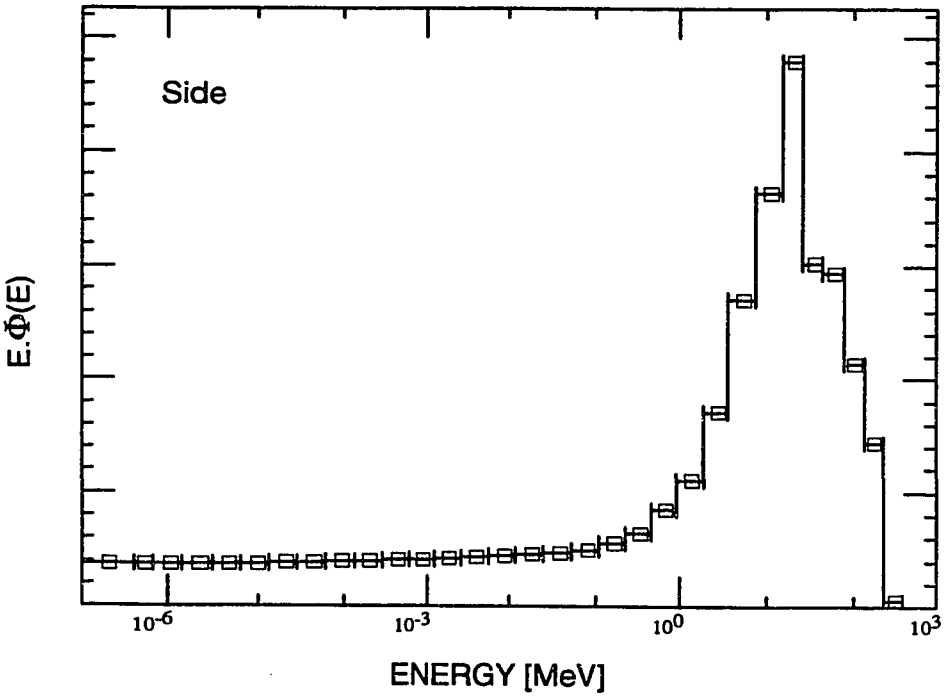

Figure 7.3: Neutron spectrum for FFTB location 1 (side of the dump).

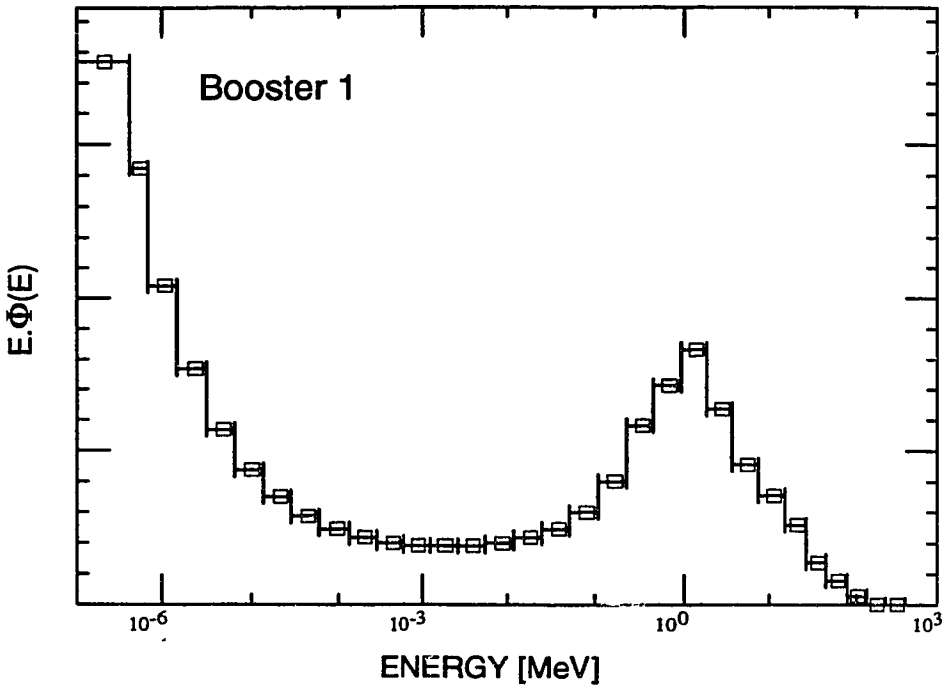

Figure 7.4: Neutron spectrum for SSRL- booster location 1 (90 degrees).

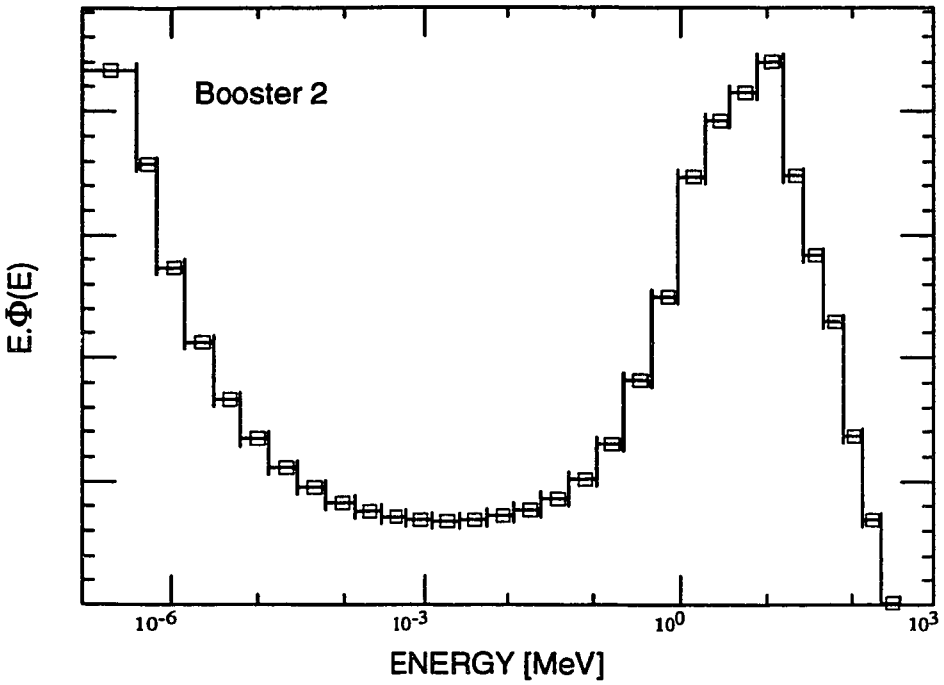

Figure 7.5: Neutron spectrum for SSRL-booster location 2 (45 degree).

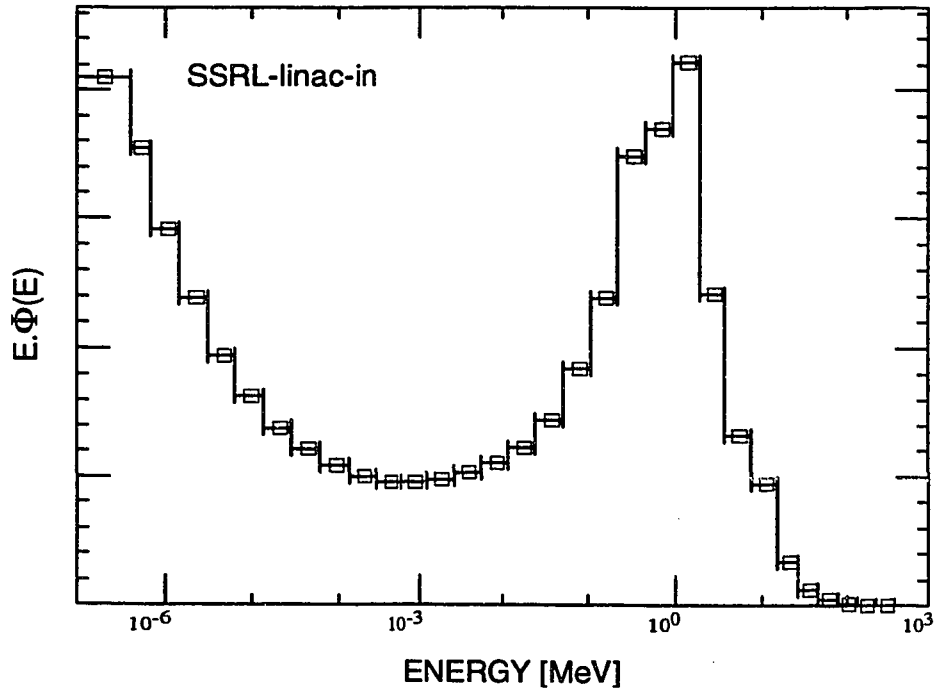

Figure 7.6: Neutron spectrum for SSRL-Linac (inside diagnostic room).

7.3 REM METER AND BONNER SPHERES RESULTS

During measurements with AB and ABPB rem meters, it was not always possible to achieve as high a number of counts as desired. The statistical uncertainty was typically between 1 to 2%, and always lower than 3%. The data were normalized with the same reference count rates as Bonner spheres. Table 7.1 contains a comparison of dose equivalent values obtained with the rem meters and the Bonner sphere system, together with other important quantities obtained from spectra unfolding. Columns 1 through 3 contain dose equivalent values for the AB and ABPB rem meters and the Bonner spheres (BS). The fourth column is the ratio of the two rem meter readings. We expect this ratio to be higher for harder spectra. The sixth column is the average energy calculated in BUNKI without considering thermal neutrons. The fluence to dose equivalent factor h_ϕ [rem cm^2] is in column 7. The last column presents the fraction of the dose equivalent from neutrons with energies above 25.81 MeV. This particular value happens to be one of the energies defining energy bins in BUNKI.

Table 7.1

Rem meters and Bonner spheres results

Location	Dose Equivalent [mrem/h]			Ratio	Av. En.	h_ϕ	H26
	AB	ABPB	BS	ABPB/ AB	[MeV]	[rem/cm^2]	[%]
FFTB-loc 3	4.8	6.2	7.7	1.3	13.8	2.3×10^{-8}	31.6
FFTB-loc 2	13.3	22.0	18.8	1.7	19.3	2.4×10^{-8}	38.9
FFTB-loc 1	.4	.9	1.4	2.2	24.5	2.9×10^{-8}	38.6
SSRL-booster1	4.5	4.8	18.9	1.1	2.0	7.4×10^{-9}	5.7
SSRL-booster2	1.8	1.7	7.1	.9	10.3	1.6×10^{-8}	22.9
SSRL-linac-in	N/A	2.9	8.8	N/A	0.9	8.5×10^{-9}	1.0

7.4 DISCUSSION

At FFTB, we observe a relatively good agreement between the BS and rem meter data. The ABPB response is always significantly higher than AB, clearly indicating a presence of a high energy portion of the spectrum. Also, the ABPB/AB ratio seems to be in agreement with the BUNKI results, being higher for harder spectra. It is a surprise to see that the spectrum on the side of the dump, approximately at 90° with respect to the beam direction, is the hardest, with a neutron fluence peak above 20 MeV. The average energy at this location is higher than at the other two locations. Since the neutrons with the highest energies from the photopion reaction are predominantly produced in the forward direction, we expected the spectrum on the side of the dump to be the softest. However, the ABPB/AB ratio, higher count rates from ^{11}C and the 12" sphere with lead relative to the other spheres seem to consistently support this finding.

The spectrum at the SSRL-booster location 1 seems to be softer than the one at SSRL-booster location 2. It has a neutron peak at approximately 1 MeV compared to the other one at 10 MeV. The average energy at location 1 is also lower than location 2, 2.01 MeV and 10.27 MeV respectively. Spectrum at location 1 has a tail extending to higher energies. However, it is not certain whether this tail is real or just an artifact of the unfolding process. With only one detector, 12" sphere with Pb, covering the high energy range, there is not enough information to determine details of the spectrum in this region. The H26 value for this spectrum is therefore subject to a large uncertainty. The spectrum at SSRL booster location 2 indicates the presence of high energy neutrons. However, the value of the ABPB/AB ratio does not support this fact, since the response of the AB rem meter is 5% higher compared to ABPB. In addition, there is again only one detector covering the high energy range. Therefore, same reservations as above apply to the H26 value for this spectrum.

As indicated in Table 7.1, dose equivalent rates from rem meters at both SSRL booster locations are significantly lower than those from Bonner spheres. We do not have any record of a source check of the rem meters during these measurements and suspect a possible error in setting the gain or the discriminator level. It is harder to make this type of mistake with the Bonner spheres, since it would be immediately noticed on the MCA as a change in the location of the neutron peak. Our confidence in the Bonner sphere

system and the SLAC response matrix is based on checks with a Cf source and measurement of known spectra behind thick shielding at CERN in April, 1995 [20].

Based on additional information, we have reason to believe that results from the Bonner spheres are correct. In 1991, Liu [19] performed measurements at SSRL-booster location #1 with passive neutron detectors and with a plastic scintillator. He also verified his measurements using a simple computer program SHIELD11. Although his measurements and calculations do not provide neutron spectra, they constitute good estimates of the dose equivalent rates from neutrons below and above 20 MeV. His results are in good agreement with our Bonner sphere results.

CHAPTER 8: CONCLUSION

We have measured neutron spectra around electron accelerators of various energies at SLAC. Unfortunately, we are not aware of any similar measurements around high energy electron accelerators, which would confirm or disagree with our results. Furthermore, the existing electron/photon transport codes do not include photoneutron generation and it was therefore impossible to support our measurements with radiation transport calculations. The situation is more favorable for proton machines, where such codes are readily available and comparison of calculations with measurements were performed [21]. However, it has been noted in scientific literature that, based on theoretical considerations, neutron spectra behind thick shielding of high energy electron and proton accelerators should be similar. This is due to the fact that, from the neutrons generated in the target either by protons or electrons, only those with the highest energies are able to penetrate through the thick shielding. As a result, the lower energy portions of neutron spectra outside the shielding are generated by these high energy neutrons in the outer layers of the shielding. This process does not depend on how the high energy neutrons were generated. Therefore, for similar shielding geometries, neutron spectra behind these shieldings should have similar shapes for proton and electron accelerators.

Based on the above arguments, the most trustworthy spectra seem to be those measured at FFTB locations 3 and 2, wooden box and hot spot. They exhibit a two peak structure similar to the measured and calculated spectra behind CERN shielding. This structure is not present in the spectrum measured at the side of the FFTB dump, with only one peak. Since this spectrum, against expectations, was the hardest, it seems necessary to repeat this measurement to confirm this result.

Bonner sphere results at the SSRL-booster agree with previous dose equivalent rate measurements by Liu. We would have more confidence in the shape of the spectra at the high energy end if the ^{11}C data were available. We hope that future measurements will confirm or improve our findings. Although ^{11}C was not included in spectra

unfolding for the SSRL-linac diagnostic room, this was due to its extremely weak signal. Since the energy of the electron beam, 120 MeV, was the lowest from all our experiments, the results might be justifiable by physical arguments. Photons with energy of 120 MeV are below the threshold for photopion neutron generation and it is likely that neutrons from the pseudo-deuteron reaction did not constitute a noticeable portion of the neutron spectrum. It is certain that the low energy portion of the spectrum leaking through the lead and concrete wall was enhanced by the presence of scattered neutrons from the walls, ceiling and floor of this small enclosure.

This work represents a first step in a comprehensive study of high energy neutron spectra around different electron accelerators at SLAC. In spite of a few flaws mentioned above, our results greatly improved the knowledge of neutron fields at this national laboratory. This significantly reduced uncertainty on neutron calibration factors for area monitors and personnel dosimeters outside shielding of electron accelerators.

BIBLIOGRAPHY

[1] Patterson, W.H. and Thomas, R.H. , 1973, "Accelerator Health Physics", (Academic Press, New York).

[2] R.L. Bramblett, R.I. Ewing and T.W. Bonner, Nucl. Instr. and Meth. 9 (1960) 1.

[3] Birattari, C. et al, "An extended range neutron rem meter", Nuclear Instruments and Methods in Physics Research A297 (1990) pp. 250-257.

[4] K.A. Lowry and T.L. Johnson "Modifications to iterative recursion unfolding algorithms and computer codes to find more appropriate neutron spectra". Memo. Rep.5340. Nav. Res. Lab., Washington, D.C. (1983).

[5] G.F. Knoll, "Radiation Detection and Measurement", pp.558-560, John Wiley&Son, Inc. 1st Edition (1979).

[6] J.B. McCaslin "A high energy neutron flux detector". Health Phys. Vol.2, pp.399-407; 1960.

[7] Hunt J.B.: "The Calibration of Neutron Sensitive Spherical Devices", Rad.Prot. Dosimetry, Vol.8 No.4, p. 239.

[8] Eisenhauer, C. "An image source technique for calculating reflection of gamma rays or neutrons". Health Phys. 11:1145-1154; 1965.

[9] Jenkins, T. M. "Simple recipes for ground scattering in neutron detector calibration". Health Phys. 39:41-47; 1980.

[10] Sun, R. K. , "Investigation of neutron scattering for a multisphere spectrometer". Health Phys. 49:325-332, 1990.

[11] Hunter, K. , private communication.

[12] V.Vylet, Thesis, Lausanne, EPFL (1987).

[13] Liu, J. C. et al, "Neutron dosimetry at SLAC: Neutron sources and instrumentation", Stanford Linear Accelearator Center, Stanford, C.A. Report No. SLAC-TN-91-3, October 1991.

[14] Sanna, R. S., "Thirty One Group Response Matrices For the Multisphere Neutron Spectrometer over the Energy Ranges Thermal to 400 MeV", Health and Safety Laboratory, U. S. Atomic Energy Commission, NY, HASL-767 (1973).

[15] Hunter, K., Thesis, "Monte Carlo Calculations of the Intensity and Energy Distribution of Ground Scattered and Room Scattered Neutrons", University of Delaware, 1994.

[16] V.Vylet, private communication.

[17] T.M Jenkins, "Radiation level at the Mark IV," SLAC-HP-64-1, Stanford Linear Accelerator Center, Stanford, CA (1964).

[18] H. Dinter and Tesh, K. "Moderatted Rem Meters in Pulsed Neutron fields," Nuc. Instrum. Method, 136, pp.389-392 (1976).

[19] J.C. Liu, private communication.

[20] Vylet & Liu, private communication.

[21] Hofert, M. and Stevenson, G. R., "The CERN-CEC high-energy reference field facility", Proc. 8th Int. Conf. on Radiation Shielding (American Nuclear society), Arlington, Texas, USA, 635-642 (1994).

APPENDIX A: A SAMPLE BUNKI INPUT FILE

```
NUMBER OF ENERGY INTERVALS ?
31
NUMBER OF DETECTORS ?
8
TYPE DETECTOR CODES ?
0
C11
2
3
5
8
10
12Pb
TYPE MATRIX NAME ?
SLAC
TYPE UNFOLDING CODE ?
SPUNIT
PUT SPECTRA IN FILE FOR PLOTTING ?
Y
1
TYPE THE HEADING
FFTB hotspot NOMAXIET  SLAC 50it no 12"
N
N
TYPE INITIAL SPECTRUM
1.0
1.0
1.0
1.0
1.0
1.0
1.0
1.0
1.0
1.0
1.0
1.0
1.0
1.0
1.0
1.0
1.0
1.0
1.0
1.0
1.0
1.0
1.0
```

1.0
1.0
1.0
1.0
1.0
1.0
1.0
0.7
0.4
0.01
0.001
TYPE: end test, smoothing factor, calibration factor, iterations before error test, and maximum number of iterations
0.2,0,1,10,50
BONNER SPHERE COUNT, % ERROR
13426,10.31
362844,5.00
29832,0.99
45774,2.92
69122,0.96
57151,0.97
43211,1.0
44471,4.15
SAVE THESE RESULTS
Y
LAST SPECTRUM
Y
CHANGE MATRIX, DETECTORS, UNFOLDING CODE AND/OR ENERGY INTERVALS ?
N

APPENDIX B: A SAMPLE OF BUNKI OUTPUT

1FFTB hotspot NOMAXIET SLAC 50it no 12"

RESPONSE MATRIX	UNFOLD CODE	MAXWELL TEMP,SHAPE	CALIB. FACTOR	SMOOTH FACTOR	PER CENT ERROR	NO. OF ITERATIONS
SLAC	SPUN	.00, .00	1.0000	.0000	2.0933	50

DETECTORS	MEASURED COUNTS	CALCULATED COUNTS	PERCENT DIFFERENCE
BARE	13426.000	13446.298	.151
C11	362844.000	360440.219	-.662
2 INCH	29832.000	29249.512	-1.953
3 INCH	45774.000	47628.273	4.051
5 INCH	69122.000	67469.312	-2.391
8 INCH	57151.000	56163.289	-1.728
10 INCH	43211.000	43278.738	.157
12+Pb	44471.000	45527.352	2.375

TOTAL FLUENCE=	7.850E+05	NEUTRONS/CM2
AVE ENERGY(LESS TH)=	1.930E+01	MEV
DOSE=	3.283E-03	RAD
DOSE EQUIVALENT=	1.880E-02	REM
QUALITY FACTOR=	5.726	REM/RAD
NRL TLD RESPONSE=	1.931	REM/REM(CF-252)
"HANKINS"TLD RESPONSE=	2.772	REM/REM(CF-252)
NEUTRAK RESPONSE=	.547	REM/REM(CF-252)
NTA RESPONSE=	.626	REM/REM(CF-252)
ANPDR-70 RESPONSE=	.459	REM/REM(CF-252)

BIN NO.	ENERGY MAX (MEV)	FLUENCE NEUT/CM2	FLUENCE N/CM2/LETH	DOSE (RAD)	DOSE EQV. (REM)	DOSE EQV. (% OF TOTAL)
1	4.140E-07	1.080E+05	6.682E+04	5.683E-05	1.244E-04	6.616E-01
2	6.826E-07	8.113E+03	3.736E+04	4.939E-06	9.995E-06	5.318E-02
3	1.445E-06	1.061E+04	3.257E+04	6.550E-06	1.330E-05	7.078E-02
4	3.059E-06	9.464E+03	2.906E+04	5.806E-06	1.177E-05	6.264E-02
5	6.476E-06	8.736E+03	2.682E+04	5.303E-06	1.072E-05	5.703E-02
6	1.371E-05	8.327E+03	2.556E+04	5.003E-06	1.008E-05	5.365E-02
7	2.902E-05	8.123E+03	2.494E+04	4.849E-06	9.707E-06	5.164E-02
8	6.144E-05	8.135E+03	2.497E+04	4.830E-06	9.591E-06	5.103E-02
9	1.301E-04	8.320E+03	2.553E+04	4.902E-06	9.659E-06	5.139E-02
10	2.754E-04	8.692E+03	2.669E+04	4.953E-06	9.762E-06	5.194E-02
11	5.929E-04	9.407E+03	2.825E+04	5.141E-06	1.016E-05	5.406E-02
12	1.234E-03	9.656E+03	3.033E+04	5.071E-06	1.004E-05	5.343E-02
13	2.613E-03	1.070E+04	3.285E+04	5.512E-06	1.092E-05	5.809E-02
14	5.531E-03	1.173E+04	3.603E+04	5.964E-06	1.183E-05	6.293E-02
15	1.171E-02	1.308E+04	4.016E+04	6.592E-06	1.320E-05	7.023E-02
16	2.479E-02	1.479E+04	4.540E+04	8.324E-06	2.239E-05	1.191E-01
17	5.247E-02	1.716E+04	5.269E+04	1.139E-05	4.610E-05	2.453E-01
18	1.111E-01	2.095E+04	6.430E+04	1.644E-05	1.000E-04	5.322E-01
19	2.237E-01	2.536E+04	8.343E+04	2.632E-05	2.105E-04	1.120E+00
20	4.508E-01	3.452E+04	1.134E+05	5.020E-05	4.888E-04	2.601E+00
21	9.072E-01	4.508E+04	1.484E+05	1.012E-04	1.078E-03	5.735E+00
22	1.872E+00	5.635E+04	1.791E+05	1.919E-04	1.976E-03	1.051E+01
23	3.679E+00	5.125E+04	1.747E+05	2.163E-04	2.048E-03	1.089E+01
24	7.408E+00	4.776E+04	1.571E+05	2.759E-04	1.945E-03	1.035E+01
25	1.492E+01	4.422E+04	1.454E+05	2.928E-04	1.818E-03	9.671E+00
26	2.581E+01	3.372E+04	1.417E+05	3.067E-04	1.469E-03	7.815E+00
27	4.465E+01	4.906E+04	2.061E+05	4.715E-04	2.173E-03	1.156E+01

28	7.725E+01	5.061E+04	2.126E+05	5.127E-04	2.385E-03	1.269E+01
29	1.336E+02	3.471E+04	1.459E+05	3.946E-04	1.744E-03	9.281E+00
30	2.312E+02	1.794E+04	7.533E+04	2.673E-04	9.933E-04	5.285E+00
31	4.000E+02	3.784E+02	1.589E+03	6.788E-06	2.406E-05	1.280E-01